climate

MDPI

Article

Analysis of Precipitation and Regionalization of Torrential Rainfall in Bulgaria

Krastina Malcheva *, Neyko Neykov, Lilia Bocheva, Anastasiya Stoycheva and Nadya Neykova

National Institute of Meteorology and Hydrology, 1784 Sofia, Bulgaria; neyko.neykov@meteo.bg (N.N.); lilia.bocheva@meteo.bg (L.B.); anastassia.stoycheva@meteo.bg (A.S.); nadya.neykova@meteo.bg (N.N.)
* Correspondence: krastina.malcheva@meteo.bg

Abstract

The increasing frequency of extreme rainfall events that cause severe damage is considered a clear sign of climate change. Therefore, analyzing these events and gaining a better understanding of the circulation patterns that form precipitation regimes and trigger torrential rainfall are crucial for developing adaptation strategies. This study aims to present a comprehensive picture of precipitation regimes in Bulgaria under contemporary climate conditions, investigate the connections between precipitation and atmospheric circulation patterns, and propose a regionalization of torrential rainfall. We used daily precipitation data collected in the period 1991–2020, along with data on hazardous rainfall warnings issued by the National Institute of Meteorology and Hydrology. To identify the circulation patterns associated with both rainy days and hazardous rainfall in Bulgaria, we applied the automated Jenkinson–Collison classification. To identify precipitation patterns, we conducted a principal component analysis in T-mode with varimax rotation and k-means clustering of component scores on both monthly normals and a dataset of 166 selected torrential rainfall days. The results, examined in the context of the existing regionalization of precipitation, highlight the climatic diversity of precipitation regimes in Bulgaria. Our findings indicate that torrential rainfall is associated with low-pressure systems and airflows mainly from the east or northeast, as well as with weak-gradient pressure fields.

Keywords: principal component analysis; Jenkinson–Collison classification; regionalization of torrential rainfall; MeteoAlarm warnings; Bulgaria

1. Introduction

Changes in the global water cycle, along with shifts in hydrological and climatic patterns due to climate change, are increasing the risks associated with extreme rainfall events and the vulnerability of affected populations [1–6]. These events can have significant socio-economic consequences, impacting infrastructure and key economic sectors [7] or triggering natural disasters, such as catastrophic floods and landslides [8,9].

Globally, observations confirm increases in extreme precipitation at daily and sub-daily timescales, as well as significant changes in precipitation patterns [1,2,10–13]. During 2011–2020, around 25% of record-breaking rainfall events can be attributed to climate change [14]. However, new studies have revealed that the rate of increase in such events varies across regions and is influenced by local factors, moisture availability, and changes in meso- and large-scale atmospheric circulation patterns [1,15,16].

Check for updates

Academic Editor: Helena A. Flocas

Received: 28 November 2025
Revised: 26 January 2026
Accepted: 28 January 2026
Published: 1 February 2026

Copyright: © 2026 by the authors. Licensee MDPI, Basel, Switzerland. This article is an open access article distributed under the terms and conditions of the Creative Commons Attribution (CC BY) license.

Recent studies focused on Europe indicate an increase in total precipitation and heavy rainfall in northern Europe. In contrast, diverse trends have been reported in the Mediterranean [12,13,17–19]. Notably, there does not appear to be a long-term trend in total precipitation, and trends observed during specific periods and in particular sub-regions can largely be attributed to internal variability in atmospheric dynamics [1,17]. However, the Mediterranean is particularly vulnerable to precipitation extremes due to complex interactions between mid-latitude and subtropical atmospheric processes, as well as the substantial influence of orography [3,20–22].

Climate change is expected to significantly impact precipitation patterns and the frequency, duration, and intensity of extreme rainfall events in the Mediterranean region by the end of the century [1,20,23]. Therefore, analyzing precipitation variability and extreme events at regional and local scales in relation to atmospheric circulation has emerged as an essential research topic. Most studies employ multivariate statistical analysis and various statistical techniques to identify precipitation and circulation patterns (e.g., [24–28]). Automated classification methods based on catalogs of circulation weather types (CWTs) [29,30] have proven to be a valuable tool to describe the regional variability of atmospheric circulation through CWT series, which, in physical terms, can explain precipitation behavior [31,32].

Over the past two decades, many studies have confirmed the applicability of automated Jenkinson–Collison (JC) classification [33,34] for analyzing the link between CWT frequency and precipitation in the Mediterranean region [34–38]. Several studies have also been conducted on neighboring Balkan countries. Putniković and Tošić [39] revealed that the cyclonic type affects seasonal precipitation over most of Serbia, while the remaining CWTs make negligible or more local contributions. Baltaci et al. [40] found that the highest probability of extreme winter rainfall in northwest Turkey occurs with northerly and cyclonic CWTs. Additionally, Akkoyunlu et al. [41] identified that convective and cyclone-driven extreme precipitation events are more common in western Turkey.

In Bulgaria, several recent studies have examined the link between extreme weather events and warnings issued by the MeteoAlarm (MA) system, using the JC classification to identify circulation conditions associated with hazardous weather [42–45]. In particular, Tsalova et al. [46] analyzed the processes related to issued warnings for intense rainfall in Sofia from May to September 2010–2019 and concluded that these events are primarily linked to cyclonic and hybrid cyclonic types. It is important to note that studies based on the subjective classification of synoptic situations have also confirmed the leading role of cyclonic circulation, specifically Mediterranean cyclones, in the occurrence of hazardous precipitation events since the 1990s [47,48].

Despite these insights, there is a lack of comprehensive studies on how atmospheric circulation is associated with precipitation patterns and the spatial variability of hazardous rainfall in Bulgaria under current climate conditions. While the existing regionalization of the country, developed in the late 1950s, provides valuable information on precipitation patterns and regimes, it does not address hazardous rainfall. Furthermore, data on meteorological alerts for hazardous rain have not yet been used in climatological studies of precipitation in Bulgaria.

In this context, the study aims to (1) provide a thorough overview of precipitation regimes in Bulgaria in light of contemporary climate conditions; (2) investigate the connections between precipitation regimes, hazardous rainfall, and atmospheric circulation; and (3) propose a regionalization specific to torrential rainfall.

To achieve these goals, we analyzed daily precipitation data from the period 1991–2020 collected from the national meteorological network. We used the automated JC classification to identify CWTs associated with both rainy days and hazardous rainfall

events (defined by the MA warning thresholds for orange and red codes issued by NIMH). We conducted T-mode PCA with varimax rotation of the principal components, followed by k-means clustering of the component scores to extract the representative seasonal and daily rainfall patterns.

To our knowledge, this approach is new to Bulgaria, as is the proposed regionalization of torrential rainfall.

2. Materials and Methods

Figure 1 illustrates the study's flowchart, detailing its stages and methodology. Section 2.1 presents the study area. The selected study period (1991–2020) is the most recent standard period for calculating climate normals, as recommended by the WMO. For the MA warning data, the relevant period is 2011 to 2020, with 2011 marking the commencement of the NIMH issuing warnings as part of the MA system.

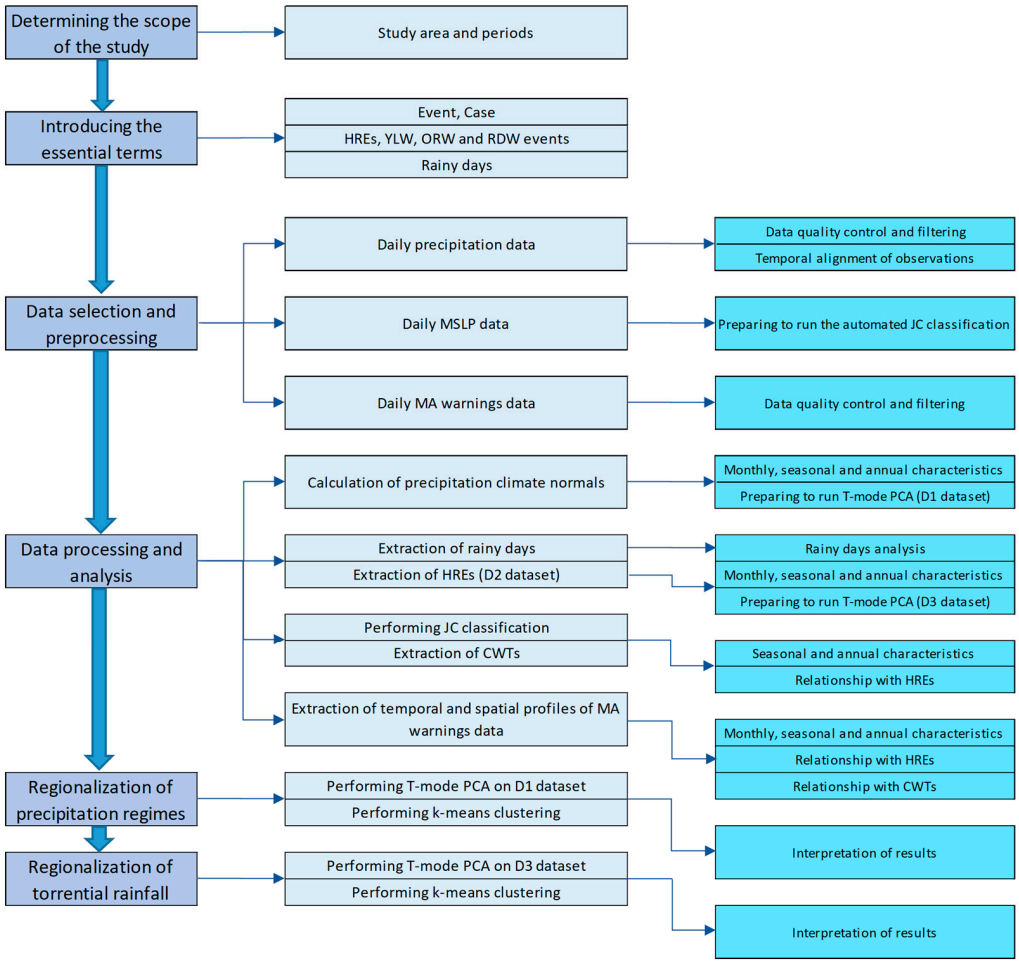


Figure 1. Flowchart of the conducted study and methodology.

We have defined the key terms utilized throughout the study as follows:

1. "Rainfall" refers to both liquid and mixed types of precipitation (i.e., rain and rain that turns to snow) due to the severe weather conditions that often accompany abundant rain-to-snow downfalls.
2. "Rainy days" refer to days with at least 1 mm of rainfall in 24 h.
3. "Heavy", "hazardous", and "torrential" rainfall: According to the criteria adopted by NIMH for issuing MA warnings, this corresponds to a 24 h precipitation exceeding the thresholds for yellow (20 mm), orange (35 mm), and red (65 mm) codes, respectively.

4. "Event" and "case": An event is a day with hazardous rainfall registered at least in one station; a case is the hazardous rain registered in an individual station; the hazardous rainfall events are referred to as HREs hereafter.
5. YLWs, ORWs, and RDWs denote the MA warnings with yellow, orange, and red codes, respectively; we also specify the events corresponding to MA warnings as YLW events (20 to 35 mm/24 h, potential hazardous conditions that may affect daily activities), ORW events (35 to 65 mm/24 h, significant conditions likely to cause inconvenience and disruptions), and RDW events (above 65 mm/24 h, extremely hazardous weather that may pose a serious risk to life and property).

In seasonal assessments, we used the standard Northern Hemisphere meteorological seasons and notations: DJF for winter—December (D), January (J), and February (F); MAM for spring—March (M), April (A), and May (M); JJA for summer—June (J), July (J), and August (A); and SON for autumn—September (S), October (O), and November (N).

In this study, we utilized three independent data sources specific to each of the outlined objectives:

1. To present a comprehensive picture of precipitation regimes in Bulgaria under contemporary climate conditions, we explored daily precipitation data from the meteorological archive of the National Institute of Meteorology and Hydrology (NIMH) for the period 1991–2020.
2. To examine the linkages among the precipitation regimes, hazardous rainfall, and atmospheric circulation over the country, we applied the automated JC classification to daily mean sea level pressure data from the NCEP-NCAR [49] reanalysis to identify CWTs.
3. To propose a regionalization of torrential rainfall, we used MA warning data on heavy rainfall and analyzed a three-component feature (precipitation amount–hazard level–circulation weather type).

Preprocessing steps for daily precipitation data and MA warnings are detailed in Sections 2.2 and 2.3.

A brief theoretical background and the particular utilization of methods in the study (JC classification, PCA, and k-means clustering) are provided in Sections 2.4 and 2.5.

The remaining stages of the study (data processing and analysis, regionalization of precipitation regimes, and regionalization of torrential rainfall) are presented and discussed consecutively in the subsections of Section 3.

The essential steps of the data processing and analysis stage include (1) developing an R-script for deriving daily weather types, employing the automated JC classification; (2) analyzing the behavior of HREs based on their frequency, extent, and contribution to the total precipitation; and (3) establishing a connection between CWTs, the occurrence of HREs, and issued MA warnings.

The regionalization of precipitation regimes and torrential rainfall is based on the sequential use of T-mode PCA with varimax rotation, followed by k-means clustering of the rotated components, applied to the relevant datasets (D1 and D3; see Section 2.2 for details).

All computations are performed using R statistical software, version 4.4.2 [50], and RStudio 2024.09.1 [51]. The maps are prepared using QGIS Desktop 3.28.5 [52]. The digital terrain model AW3D30 from the Japan Aerospace Exploration Agency [53] is used to prepare the hypsometric map of Bulgaria. The spatial interpolation of annual precipitation normals is performed using the R packages "automap" [54] and "terra" [55].

2.1. Study Area

Bulgaria is situated in Southeastern Europe, in the eastern part of the Balkan Peninsula, between 44°13′ and 41°14′ north latitude and 22°40′ and 28°37′ east longitude. A notable feature of the country is its diverse topography (Figure 2, top). The climate of Bulgaria is temperate continental, with a transition towards Mediterranean-type climates. According to the climate classification of Köppen–Geiger [56], three climate types can be distinguished (Figure 2, bottom left): temperate, with hot (Cfa) or warm (Cfb) summers but without a dry season, or Mediterranean-type—with dry and hot (Csa) or warm (Csb) summers; boreal, without a dry season—with warm summers (Dfb) or cool summers (Dfc); and alpine tundra-type (ET).

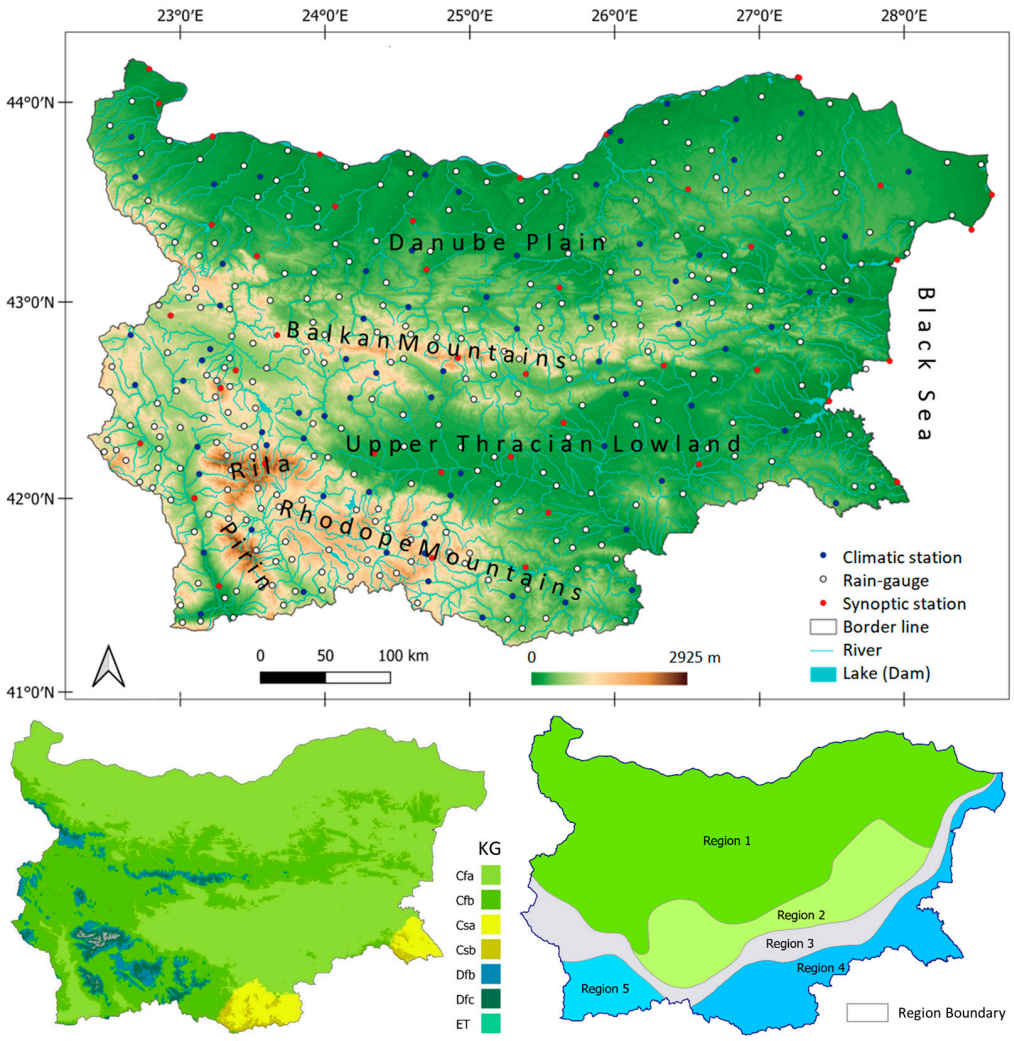


Figure 2. (**Top panel**): Location of the 355 meteorological stations of the national meteorological network (synoptic, climatic, and rain-gauge) on the background of the hypsometric map of Bulgaria. (**Bottom-left panel**): Köppen–Geiger climate classification (KG) for 1991–2020 [57]. (**Bottom-right panel**): Regionalization of precipitation regimes in Bulgaria. The regions with different precipitation regimes are labeled Region 1 to Region 5.

Climate change, evident in Southeastern Europe since the mid-1980s [58,59], has altered not only temperature and seasonal precipitation patterns but the distribution of the main climate subtypes over 36% of the country's territory [57,60]. The predominant subtype in 1991–2020 is Cfa (59.1%), followed by Cfb (30.9%). The influence of Mediterranean climates is more pronounced in the southernmost regions.

The existing climatic regionalization of precipitation regimes in the country (Figure 2, bottom right) was conducted in the late 1950s and has recently been used to study changes in the distribution of dangerous precipitation (>60 mm/24 h) [61]. The country is divided into five precipitation regions. The largest one (Region 1) features continental climates, with a pronounced summer precipitation maximum and a winter minimum. In Regions 2 and 3, which represent a transition zone between continental and Mediterranean climates, monthly precipitation is more evenly distributed, without pronounced peaks. In Region 4 (encompassing parts of the Rhodope Mountains, the southeastern low-altitude region, and a relatively narrow area along the Black Sea coastline) and Region 5 (covering the southwestern corner of the country), the Mediterranean precipitation regime, characterized by a late autumn or winter maximum, is well expressed.

Regarding circulation conditions influencing precipitation regimes over the same historical period, Stanev et al. [62] used a subjective classification of daily synoptic situations. They found that Mediterranean cyclones (most frequent from November to May) significantly impact the precipitation in southern Bulgaria, while Atlantic cyclones (most frequent from February to June, with a peak in May) have a substantial influence on precipitation in northern Bulgaria. In autumn, increased cyclonic activity over the Eastern Mediterranean and the Black Sea, driven by the more frequent advection of Arctic air masses, considerably impacts precipitation in the eastern part of the country. Cyclonic circulation occurs in about 20% of days per year. Convective rainfall is often associated with weak-gradient pressure fields, which appear on 22% of days per year, most frequently in the summer.

Unlike total precipitation, hazardous rainfall in Bulgaria exhibits significant variability and an irregular spatiotemporal distribution, with 24 h amounts that can exceed 100 mm. It is not unusual for monthly normals to be exceeded by 2 or more times during single events [63].

2.2. Precipitation Data

We used daily precipitation data collected from meteorological stations across the national meteorological network, operated by NIMH (Figure 2, top panel). Key metadata for synoptic and climatic stations can be found in Table A1 of Appendix A. The rain-gauge network is sufficiently dense to allow for plausible spatial analyses (each station represents precipitation over an average area of approximately 320 km^2).

The initial dataset consists of daily precipitation data collected from 355 meteorological stations, covering the period from 1 January 1991 to 31 December 2020 (10,958 days). The data underwent primary expert control for gaps and errors and were processed in accordance with quality control procedures following the WMO guidelines [64]. To improve alignment between daily climatological precipitation observations and corresponding daily CWTs and MA warnings, a one-day backshifting method was employed (see Appendix B for details).

Rainy days were identified by filtering the preprocessed dataset to include all days with rainfall $\geq$1 mm/24 h.

Monthly precipitation normals (1991–2020) were computed in accordance with the WMO guidelines [65]. The resulting dataset (D1) represents a matrix (355 $\times$ 12) including the calculated monthly normals for all 355 stations.

HREs were identified by filtering the preprocessed dataset using the ORW threshold (35 mm/24 h). Additionally, we excluded all stations with long periods of missing data (i.e., one month or more). As a result, we selected 329 stations and extracted 2060 HREs. We developed a dataset (D2) that includes essential HRE parameters: date, rainfall amounts by station, the number of affected stations, their distribution by event type (ORW and RDW), and average rainfall amounts by event type.

We analyzed the behavior of HREs based on their frequency, extent, and contribution to the total precipitation. All computations were performed on the D2 dataset. By definition, each HRE is associated with a unique date. Thus, the number of days equals the number of events at the monthly and annual scales (i.e., their frequency). The most natural measure of the HRE's extent is the number of stations that recorded precipitation exceeding 35 mm/24 h during the event, as the study solely uses station data. The contribution of HREs to monthly and annual precipitation totals provides a valuable measure for evaluating their impact within the climatological context.

To identify torrential rainfall patterns, we selected 166 days from the D2 dataset with rainfall exceeding 65 mm/24 h for at least three stations. Applying this constraint helped us avoid including highly localized events. The resulting dataset (D3) was extracted from the preprocessed initial dataset and organized as a T-mode matrix (329 × 166) comprising rainfall data from 329 stations for the 166 selected days, regardless of precipitation amounts across stations.

2.3. MeteoAlarm Heavy Precipitation Warnings Archive

NIMH is the primary institution in Bulgaria responsible for monitoring hydrometeorological conditions and issuing weather-related warnings for a variety of events, such as heavy rainfall and snowfall, strong wind, extreme temperatures, heat waves and cold spells, thunderstorms, fog, and coastal events [66]. The color-coded warnings indicate the severity of the event following the MeteoAlarm system notations [67].

The necessary information for significant/intense precipitation (rain or snow) and accompanying phenomena such as thunderstorms and hail has been extracted by day from the archive of issued warnings for hazardous phenomena. The created dataset contains information about the date (year–month–day format) and issued MA code (if there is one) for each of the 28 administrative districts in the country. Criteria for issuing warnings for heavy precipitation are shown in Table 1.

Table 1. Criteria adopted by NIMH for issuing warnings for heavy precipitation.

YLWs	ORWs	RDWs
20–35 mm/24 h or intense rain $\leq$ 30 mm/6 h	35–65 mm/24 h or intense rain > 30 mm/6 h	>65 mm/24 h

2.4. Objective Weather Type Classification

The objective Lamb weather type classification proposed by Jenkinson and Collison [33,34] (see Appendix C for details) was applied to identify circulation weather types over Bulgaria. Daily mean sea level pressure (MSLP) data on a 2.5° × 2.5° grid from the NCEP–NCAR reanalysis dataset were used for this purpose [68]. The dataset covers the European sector (5° E–45° E, 25° N–60° N) and spans the same period as the precipitation data. The R package "jcext" [69] was employed to derive daily CWTs, resulting in the identification of 27 circulation weather types (Table 2). These weather types were further regrouped into 11 basic types (shown in bold italics) by weighting and transforming the 16 hybrid types into the corresponding directional and cyclonic/anticyclonic types, following Jenkinson and Collison [34].

Table 2. JC classification of CWTs. Following [34], the atmospheric circulation characterized by weak flow (weak pressure gradient) is referred to as the low flow (LF); the 11 basic types are shown in bold italics.

Anticyclonic		Directional		Cyclonic		Low Flow
A	Anticyclonic			***C***	Cyclonic	***LF***
AN	Anticyclonic Northerly	***N***	Northerly	CN	Cyclonic Northerly	
ANE	Anticyclonic Northeasterly	***NE***	Northeasterly	CNE	Cyclonic Northeasterly	
AE	Anticyclonic Easterly	***E***	Easterly	CE	Cyclonic Easterly	
ASE	Anticyclonic Southeasterly	***SE***	Southeasterly	CSE	Cyclonic Southeasterly	
AS	Anticyclonic Southerly	***S***	Southerly	CS	Cyclonic Southerly	
ASW	Anticyclonic Southwesterly	***SW***	Southwesterly	CSW	Cyclonic Southwesterly	
AW	Anticyclonic Westerly	***W***	Westerly	CW	Cyclonic Westerly	
ANW	Anticyclonic Northwesterly	***NW***	Northwesterly	CNW	Cyclonic Northwesterly	

In this study, however, we employed an alternative regrouping that allows us to differentiate between directional and hybrid types, considering all anticyclonic advective types as one group (Ad) and all cyclonic advective types as another group (Cd). We also used notations A* and C*, considering the general anticyclonic and cyclonic circulation features.

The following quantitative measures were used to characterize the association between HREs and CWTs:

1. CWT frequency (in days) represents the number of HREs corresponding to a given CWT at the monthly and annual scales.
2. The number of CWT cases equals the number of HRE cases corresponding to a given CWT at the monthly and annual scales.
3. The contribution of CWTs to precipitation (in mm) is estimated as the weighted sum of the average precipitation from individual HREs corresponding to a given CWT on a monthly and annual scale.
4. The proportion of CWTs per month, season, or year (in %) is equal to the frequency of CWTs divided by the corresponding number of HREs during the study period.

2.5. Principal Component and Cluster Analysis

Principal component analysis (PCA) is a technique for data dimensionality reduction, visualization, and denoising through transforming correlated variables into new, uncorrelated variables called principal components. This method is widely used in climate studies to reduce the temporal and spatial dimensions of climate data to reasonable, physically interpretable abstractions [70–72]. The transformation is based on eigenvalue–eigenvector decomposition of the data (or covariance) matrix. The eigenvectors, or loadings, define the directions of maximum variance, while the corresponding eigenvalues quantify the variance captured. The principal components themselves are calculated as scores from linear combinations of the original variables. In the atmospheric sciences, the standard PCA (S-mode PCA) processes temporal observations as rows and spatial locations as columns, revealing leading spatial patterns of variability. In contrast, T-mode PCA transposes the

data matrix to highlight dominant temporal patterns across space, such as atmospheric circulation regimes.

K-means clustering groups similar data points into distinct clusters [73,74]. When PCA and k-means are combined, PCA is first used to transform high-dimensional data into a smaller set of uncorrelated components that capture most of the variance, reducing noise and redundancy. This preprocessing step makes k-means clustering more effective at identifying meaningful and well-separated groups. Consequently, PCA combined with k-means clustering is a suitable statistical approach for filtering and classifying climate data, as it reveals underlying structures and patterns while improving visualization, interpretability, and computational efficiency.

In this study, seasonal precipitation patterns were derived from the D1 dataset, whereas the main torrential rainfall patterns were derived from the D3 dataset.

The k-means procedure in the R package "NbClust" [75] was used to identify zones with similar precipitation characteristics after T-mode PCA of the D1 dataset. An optimal number of clusters was determined using the validation indices from the "NbClust" package, consistent with the spatial patterns of the rotating PCs and the existing precipitation regionalization. The process of delineating regions with coherent precipitation from the clustered points was carried out entirely in QGIS through the following steps:

1. Creating Thiessen Polygons from the clustered point layer.
2. Overlaying the resulting polygon layer with the altitudinal climate zones.
3. Adjusting the clusters according to the new partitioning of the Thiessen Polygon layer and subsequently merging all polygons with the same cluster number.
4. Mapping the obtained clusters using the simple contouring and smoothing method in QGIS [76].

The homogeneity of regions was validated using statistics for monthly and seasonal precipitation totals derived from observational data [77].

Similarly, we conducted k-means clustering on varimax-rotated PC scores after T-mode PCA of the D3 dataset using the "NbClust" package to identify the main spatial patterns of torrential rainfall. These clusters were visualized in QGIS through the following steps:

1. Creating Thiessen Polygons from the clustered point layer.
2. Adjusting the clusters and subsequently merging all polygons with the same cluster number.
3. Mapping the obtained clusters using the simple contouring and smoothing method in QGIS.

3. Results and Discussion

3.1. Data Processing and Analysis

3.1.1. Precipitation Climate Normals (1991–2020)

Annual precipitation normals range from 450 to 550 mm (in particular, regions of the Danube Plain, Upper Thracian Lowland, and Black Sea coast) to 900–1200 mm in the mountainous areas (Figure 3). In the mountains, precipitation increases almost linearly with altitude up to around 2000 m. The country's average annual precipitation is 663 mm.

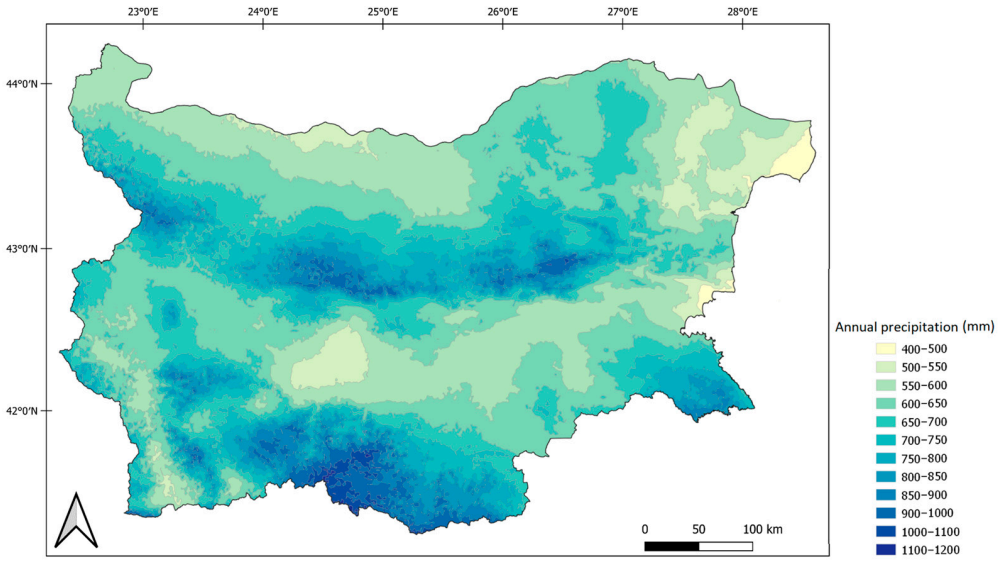


Figure 3. Spatial distribution of annual precipitation normals for the period 1991–2020.

Monthly precipitation normals (Figure 4) show significant spatial and intra-annual variability. At around 70% of stations, monthly precipitation does not exceed 60 mm, but no region experiences completely dry months. Furthermore, across all seasons, 1–3% of stations have monthly normals exceeding 100 mm.

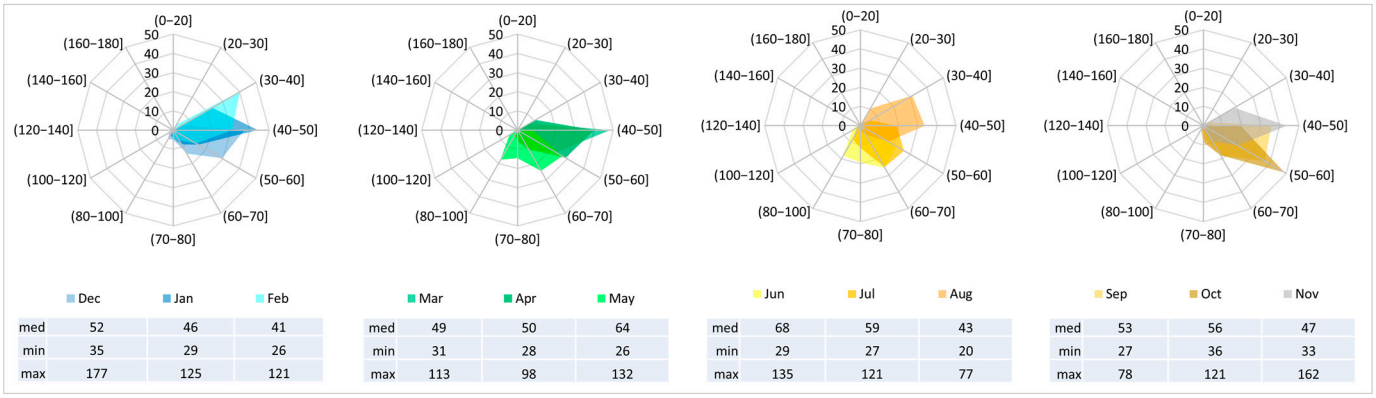


Figure 4. Monthly precipitation normals for 1991–2020 by season (unit: mm); vertical axes indicate the percentage of stations whose normals fall within the specified intervals: (0–20], (20–30], (30–40], . . ., (160–180] mm; "med", "min", and "max" denote the country median, minimum, and maximum values of monthly normals, respectively.

3.1.2. Rainy Days (1991–2020)

The annual number of rainy days and daily rainfall amount, averaged across the country, are 63 days and 8.8 mm/24 h, respectively. The rainy days occur most frequently in May (8) and June (7), and the least in January (3). Regarding the upper tail of the rainfall distribution on rainy days, the country median values of the calculated 90th, 95th, and 99th percentiles at stations are 19.8 mm, 26.6 mm, and 45.4 mm, respectively. Notably, the threshold values for issuing MA warnings with orange and red codes correspond to the country medians of the 97.5th and 99.7th percentiles.

3.1.3. HREs (1991–2020)

The monthly distribution of HREs in the period 1991–2020 shows apparent seasonality, with a peak between May and July (the absolute maximum is 24 days in June, 2019) and a minimum (including zeros) during the cold season (Figure 5, left). The year with the most HREs is 2014, followed by 2005. Monthly averages range from two days in February to 12 days in June. In terms of seasonal distribution, winter accounts for 13.2%, spring for 22.6%, summer for 43.1%, and autumn for 21.1% of HREs.

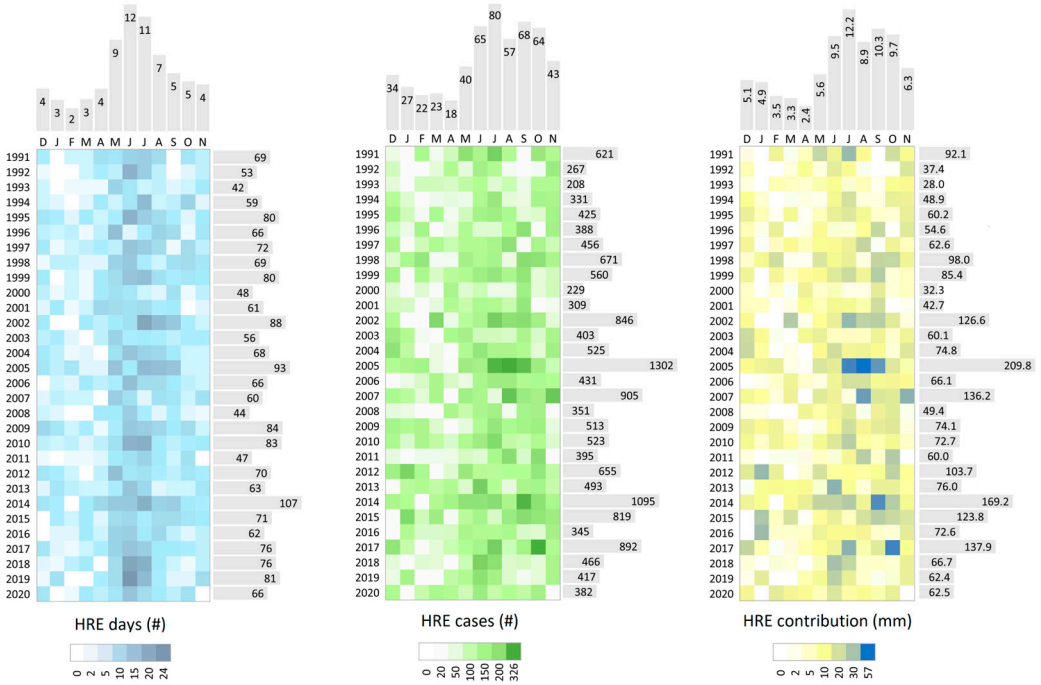


Figure 5. Calendar heatmaps of HRE days (**left panel**), HRE cases (**middle panel**), and HRE contribution to monthly precipitation (**right panel**), with added histograms for monthly averages and annual totals over the period 1991–2020.

Both monthly and annual distributions of HRE cases show a high variability (Figure 5, middle). Still, they are more frequent in summer and autumn. Monthly averages ranged from 18 cases in April to 80 cases in July. The highest number of HRE cases was observed in 2005, followed by 2014.

The HRE contribution to the monthly precipitation was calculated as a weighted monthly sum of the average rainfall of individual HREs. The weight of each HRE was determined by the ratio of the number of affected stations to the total number of stations. Naturally, the patterns of this measure follow those of HRE cases, and they also show a higher variability (Figure 5, right). The highest monthly HRE contribution has been recorded since 2005. The average monthly contribution ranges from 2.4 mm in April to 12.2 mm in July.

Figure 6 presents another view of the HREs' behavior over the years, showing the average monthly number of cases per event as a percentage of the total number of stations.

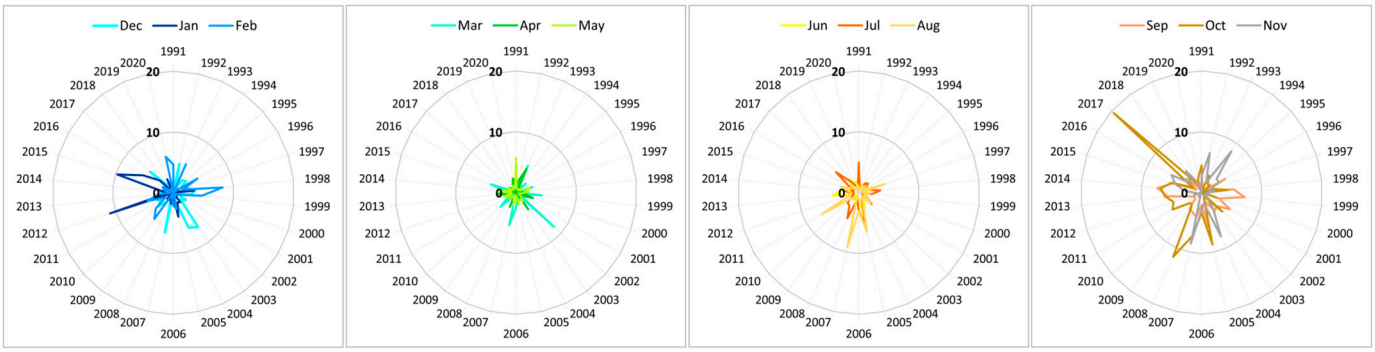


Figure 6. Average monthly number of cases per event as a percentage of the total number of stations in the period 1991–2020 (in %).

In spring and summer, more local HREs prevail, commonly due to the higher convective activity during these seasons [21,24,62]. So, the HREs' extent rarely surpasses 5–6%. During autumn and winter, the increase in cyclonic activity is associated with rising frontal precipitation [24,62], and the HRE extent falls more frequently within the 6–10% interval. The top-rated months in the study period are October 2017 (19.6%), October 2008 (11.6%), January 2012 (11%), and January 2015 (9.7%).

The percentage contribution of HREs to annual precipitation in stations with precipitation below the country average ranges from 4% to 21.4%, with a median of ~10%. The HRE contribution increases smoothly with annual precipitation, reaching a median of 18.4% for stations with the highest annual normals (Figure 7, left). The average monthly contribution of HREs across stations for the period 1991–2020 (Figure 7, right) shows a clear increase during the warm season. Median values from November to April are below 4 mm, while those from May to October range between 5 mm and 12 mm.

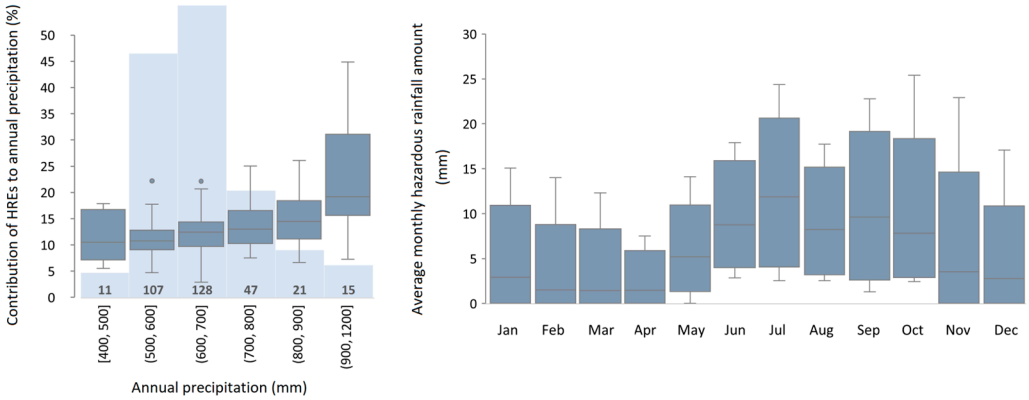


Figure 7. (**Left panel**): Box plot of the percentage contribution of HREs to annual precipitation by stations, grouped according to calculated annual precipitation normals (light blue histogram; the number of stations in each group is also shown). (**Right panel**): Box plot (5th to 95th percentiles) of the average HRE contribution to monthly precipitation across stations in the period 1991–2020.

Our results, showing clear seasonality and an apparent increase in HREs during the warm season at most stations, are consistent with those of Mastrantonas et al. [21]. They conclude that, while most extreme precipitation events in the Eastern Mediterranean occur during the winter, the Balkans exhibit an opposed pattern. Spring and summer are the two seasons with the highest frequency of such events across most inland areas, likely associated with different large-scale patterns, as the influence of the Mediterranean Sea is weaker. These findings highlight the importance of elaborating regionalization specific to torrential rainfall in Bulgaria.

3.1.4. JC Classification and Extraction of CWTs (1991–2020)

Using the developed R script, we derived the distribution of all 27 CWTs in the study period by date. Regarding the most commonly occurring atmospheric circulation patterns, the seasonal and annual distributions of the 11 basic CWTs (as defined in [34]) mostly correspond to those reported by Stanev et al. [62].

On an annual scale, the dominant CWT is the anticyclonic type (A, 25.9%), as seen in Figure 8. The low-flow circulation (LF) exhibits a distinct seasonality, with a minimum in winter (7.3%) and a maximum in summer (29.7%). The frequency of the cyclonic type reflects the number of cyclones that pass through the country, with a maximum in spring (14.9%).

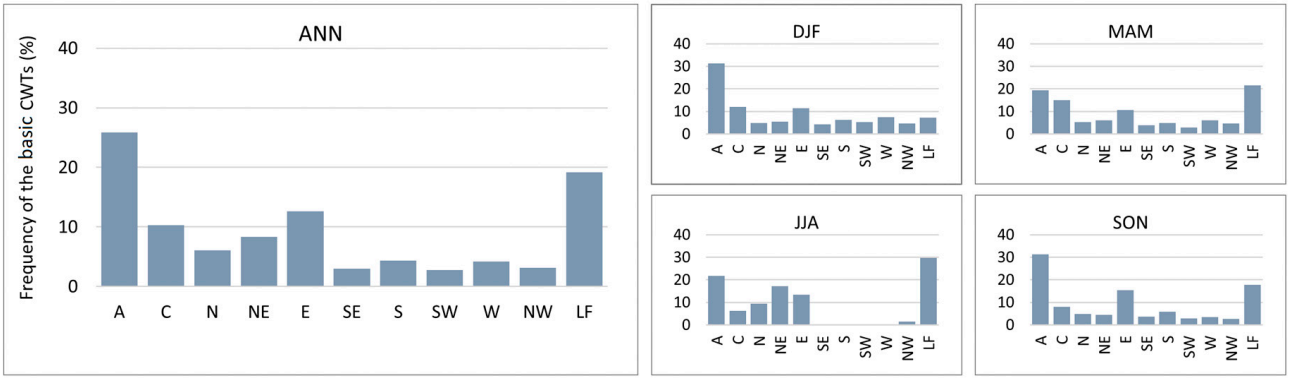
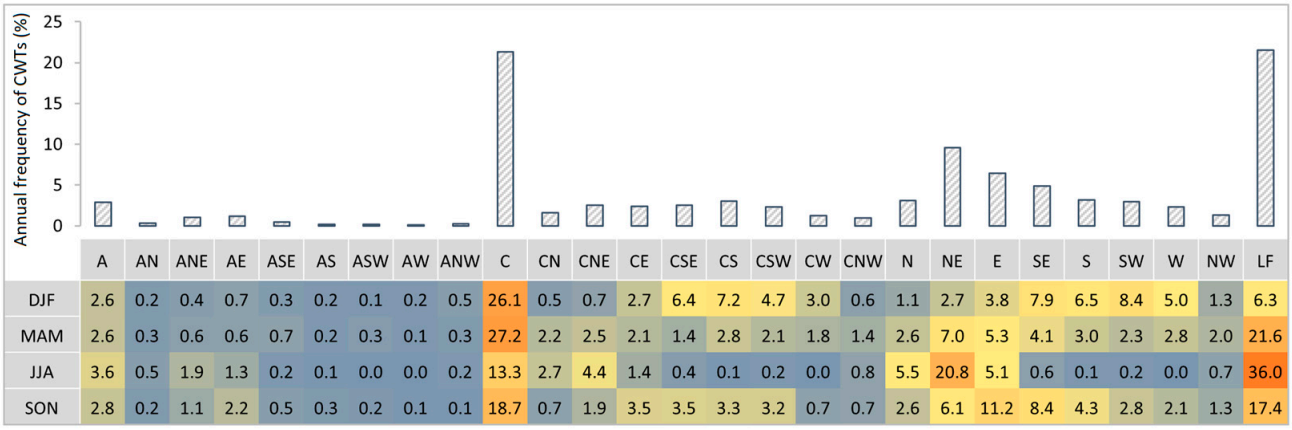


Figure 8. Average seasonal and annual (ANN) frequencies (in %) of the 11 basic CWTs for the period 1991–2020; vertical axes are the same across plots.

Among directional CWTs, the most frequent are NE (17.2%) in summer and E (15.3%) in autumn. The frequency of westerlies (NW, W, and SW) reaches 15.8% during the cold season (October–March), while the easterlies (NE, E, and SE) prevail with 26.4% during the warm season (April–September).

It is not surprising that these results largely agree with the findings of Nita et al. [78] for Romania at both the seasonal and annual scales.

Analyzing circulation types associated with rainy days, we identified a small number of CWTs that contribute significantly (approximately 64%) to rainy day occurrence (Figure 9).



	A	AN	ANE	AE	ASE	AS	ASW	AW	ANW	C	CN	CNE	CE	CSE	CS	CSW	CW	CNW	N	NE	E	SE	S	SW	W	NW	LF
DJF	2.6	0.2	0.4	0.7	0.3	0.2	0.1	0.2	0.5	26.1	0.5	0.7	2.7	6.4	7.2	4.7	3.0	0.6	1.1	2.7	3.8	7.9	6.5	8.4	5.0	1.3	6.3
MAM	2.6	0.3	0.6	0.6	0.7	0.2	0.3	0.1	0.3	27.2	2.2	2.5	2.1	1.4	2.8	2.1	1.8	1.4	2.6	7.0	5.3	4.1	3.0	2.3	2.8	2.0	21.6
JJA	3.6	0.5	1.9	1.3	0.2	0.1	0.0	0.0	0.2	13.3	2.7	4.4	1.4	0.4	0.1	0.2	0.0	0.8	5.5	20.8	5.1	0.6	0.1	0.2	0.0	0.7	36.0
SON	2.8	0.2	1.1	2.2	0.5	0.3	0.2	0.1	0.1	18.7	0.7	1.9	3.5	3.5	3.3	3.2	0.7	0.7	2.6	6.1	11.2	8.4	4.3	2.8	2.1	1.3	17.4

Figure 9. Average seasonal and annual frequencies (in %) of all 27 CWTs associated with rainy days in the period 1991–2020. We used conditional formatting to visualize the CWT contribution to rainy-day occurrences, ranging from 0% (grey-blue) to 36% (dark orange).

The cyclonic (21.3%) and low-flow (21.6%) circulation types are dominant, followed by three directional types: northeasterly (9.6%), easterly (6.4%), and southeasterly (4.9%). Generally, 51.7% of rainy days in winter, 43.7% in spring, 23.2% in summer, and 36.3% in autumn occurred under cyclonic circulation (C or Cd).

The contribution of weather types to the intra-annual distribution of HREs is presented by the monthly CWT frequencies (Figure 10, left). The overall occurrence of the grouped anticyclonic (A*) and cyclonic (C*) types in the period 1991–2020 is 102 and 768 days, respectively. The most frequent directional CWTs during the warm season are NE (248 days) and E (144 days). During the cold season, the most frequently occurring directional CWTs are SE (75 days), SW (59 days), and S (55 days). The cyclonic circulation (C*) exhibits a high frequency throughout the year, with a maximum in May (105 days) and a minimum in February (44 days). The low-flow circulation (LF) is the second most frequent type (534 days). The anticyclonic circulation (A*) reaches maxima in June (27 days).

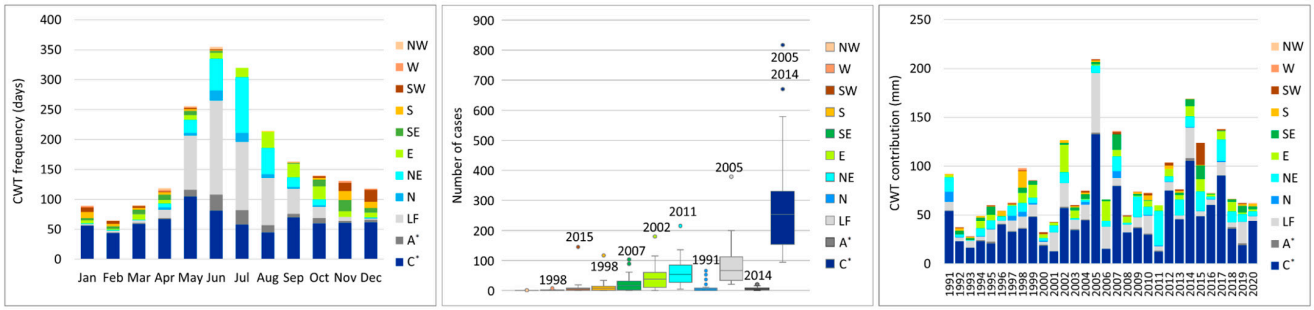


Figure 10. (**Left panel**): Monthly CWT frequency. (**Middle panel**): Box plot of the annual number of CWT cases. (**Right panel**): CWTs' contribution to annual precipitation (in mm); A* and C* represent the summarized frequencies of all anticyclonic and cyclonic types, respectively; study period: 1991–2020.

The annual number of cases reflects the influence of CWTs on the extent of HREs, as shown in Figure 10 (middle), along with the years of achieved maxima. Two CWTs (NW and W types) had a negligible occurrence during the study period (fewer than two per year). Most of the achieved maxima occur in certain "wet" years in Bulgaria and the Balkans [63]. The annual number of cases exhibits a significant variability for all CWTs, with median values ranging from 0 (for NW and W types) to 254 under cyclonic circulation conditions.

Figure 10 (right) illustrates how different CWTs contribute to annual precipitation. In the years with the highest proportion of HREs, specifically 2005 and 2014, cyclonic and low-flow circulation were the most significant contributors to annual precipitation. In certain years, the contribution of individual directional CWTs peaked at 3–5% of the country's annual precipitation normal (e.g., E type in 2002, SE type in 2007, NE type in 2011, and SW type in 2015).

Figure 11 shows the country-averaged seasonal frequency of CWTs associated with HREs in the individual stations. Cyclonic type is the most frequent in spring (44.9%), winter (44.1%), and autumn (30.5%). In summer, LF (27.5%) and NE (22.3%) types are the most frequent.

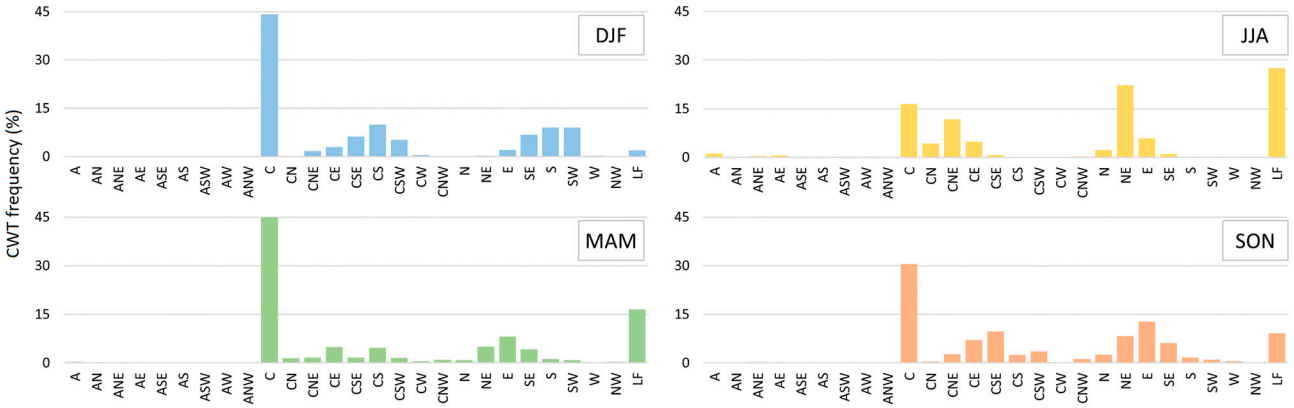


Figure 11. Seasonal frequency of CWTs associated with HREs (in %) for 1991–2020, averaged across stations.

Among the directional CWTs, the most frequent during winter are SW, S, and SE, while easterlies (NE, E, and SE) are the most frequent during spring and autumn. Anticyclonic CWTs are least frequent, with a combined maximum of 2.3% in summer, but individually below 0.5%. The respective annual frequencies of anticyclonic, cyclonic, directional, and low-flow circulation are approximately 1%, 53%, 30%, and 16%.

Our findings align with several regional studies that clearly indicate the significant influence of cyclonic circulation, weak (low) flows, and various advective circulation types on precipitation and heavy rainfall patterns over the Balkan Peninsula [21,24–26,41,46]. Three major factors determine precipitation behavior in the region: (1) the intense cold season activity of Mediterranean depressions; (2) the seasonal northern polar front displacement and thermal convection during the warm season [79]; and (3) the notable orographic diversity, resulting in very different precipitation patterns over relatively short distances [80].

Lionello et al. [81] found that the most intense features in the cyclone spatial distribution over the Mediterranean are linked to well-defined branches and areas where cyclogenesis is frequent, including the north part of the Aegean Sea and the Black Sea. The results show significant negative trends of cyclone frequency in spring and positive trends in summer. The analysis conducted by Caian et al. [82] revealed that Mediterranean-origin cyclones dominate over Southeastern Europe and are the primary source of rainfall extremes. Moreover, their findings point to an increasing number of warm season extreme cyclone tracks in the south and southeast parts of the domain, including Bulgaria. During the cold season, changes were of a smaller amplitude, decreasing in the south.

In most of the Balkans, spring and summer are the seasons with the highest frequency of extreme rainfall events, often linked to thermal low-pressure systems over the region and enhanced by orography [21]. Mesoscale circulation systems can be considered a factor controlling the initiation and development of convection above complex terrain under weak synoptic flows. Topography is crucial for triggering and modifying convection [83].

3.1.5. MA Warnings for Heavy Rainfall (2011–2020)

The issued MA warnings from 2011 to 2020 comprise 370 days with a yellow code, 100 days with an orange code, and 10 days with a red code. Figure 12 (top right) illustrates the significant interannual variability in the number of issued warnings.

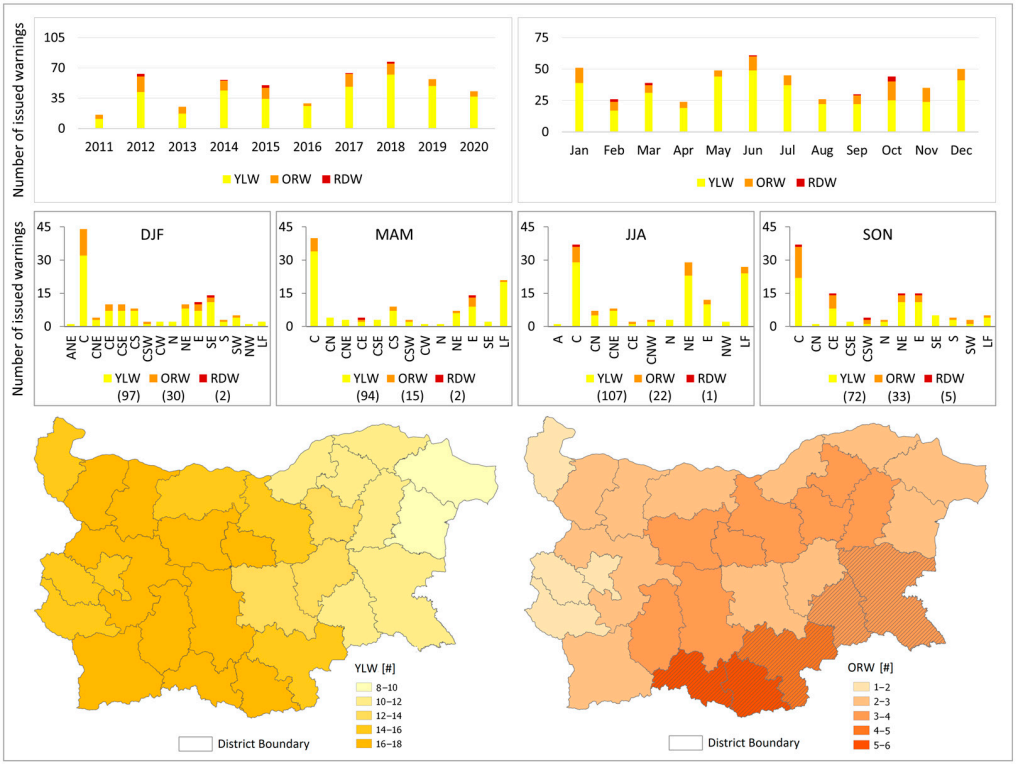


Figure 12. (**Top panel**): Number of issued MA warnings for heavy precipitation in the period 2011–2020 by year (**left**) and month (**right**). (**Middle panel**): Number of issued warnings by CWT and season; the overall seasonal number of YLWs, ORWs, and RDWs is shown in parenthesis. (**Bottom panel**): Annual frequency of YLWs (**left**) and ORWs (**right**) for heavy precipitation in the period 2011–2020 by district; the districts with at least one RDW are hashed on the ORW map.

Additionally, there is a notable decline in the number of warnings issued as the warning severity increases. The distribution of YLWs shows a summer maximum of 107 days. For ORWs, a higher frequency is found in winter (43 days), and RDWs reach a maximum of 5 days in autumn (Figure 12, top left).

In analyzing the distribution of issued warnings by circulation type from 2011 to 2020, we identified several CWTs associated with a higher number of heavy rainfall alerts across seasons (see Figure 12, middle). Most YLWs are associated with cyclonic circulation (up to 34 alerts for C-type in spring, and up to 27 alerts for Cd-types in winter). Among the directional CWTs, the most frequent are easterlies (NE, E, and SE), with a maximum of 23 alerts for NE in summer. The warnings under low-flow circulation are characteristic only of spring and summer. ORWs show a similar seasonal distribution by circulation types, with a maximum of 14 alerts for C-type in autumn and 9 alerts for Cd-types in winter. In contrast, RDWs are obviously concentrated in autumn and are mostly associated with advective types (cyclonic or directional).

The annual frequency of YLWs exhibits a well-defined spatial pattern, with a decreasing gradient from west to east. Most districts in western Bulgaria received between 14 and 18 YLWs annually, whereas this number was typically 8–14 in eastern Bulgaria (Figure 12, bottom left). In contrast, the ORW and RDW patterns exhibit zonality, with clearly distinguishable groups of districts in northern and southern Bulgaria receiving over three ORWs per year. Moreover, all RDWs were issued only for a few districts in the southern and southeastern parts of the country (Figure 12, bottom right).

Comparing the average number of YLW, ORW, and RDW events for the periods 2011–2020 and 1991–2020, we found no substantial changes in the frequency of any event type over the last decade of the study period, which allows us to use the results from the

analysis of MA warnings in the further regionalization of torrential rainfall for the period 1991–2020.

Figure 13 shows the month with the highest number of HREs at each station over the study period, with the size of the circles proportional to the magnitude of the maximum. In the largest number of stations, the maximum number of HREs occurs in July (125), followed by October (71), June (63), and September (61).

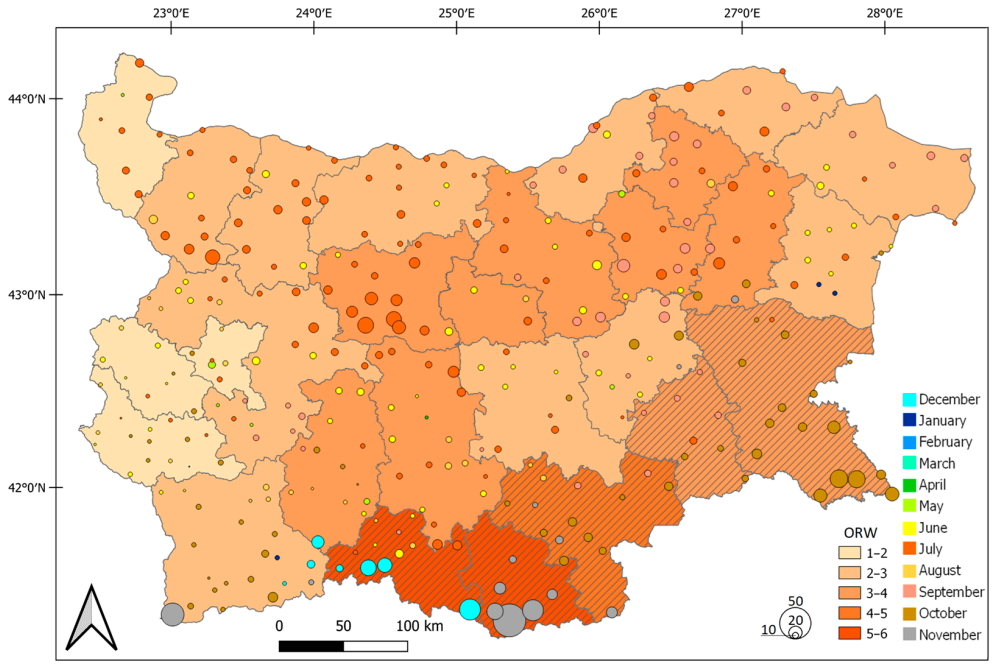


Figure 13. The maximum number of HREs in each station by month over the study period (1991–2020) on the background of the average annual number of ORWs (Figure 12, bottom right); for tied maximum values, the calendar month of their first occurrence is indicated; the size of the circles is proportional to the magnitude of maxima.

Generally, this complex HRE characteristic corresponds to the ORWs' spatial distribution: the smaller the HRE maximum per station, the fewer ORWs are present in the respective district.

To summarize the data processing and analysis stage, we should emphasize the high consistency of the results obtained across the three independent datasets. From the rainy days through precipitation climate normals to HREs, along with CWTs and MA warnings, all calculated measures exhibit consistency. Indeed, the upper percentiles of the rainy day distribution confirmed the extremity of rainfall exceeding the thresholds for ORWs and RDWs. The HRE measures indicated a clear seasonality, which can be tracked and linked to MA warnings and interpreted through the CWT series.

3.2. Regionalization of Precipitation (1991–2020)

We applied PCA in T-mode with varimax rotation to the D1 dataset to identify the main patterns in precipitation seasonality (see Appendix D for details).

Component V1, which explains 45% of the total variance, shows a peak loading for winter precipitation (Figure 14, top). The highest scores are associated with stations in the southern and southeastern regions of the country, where Mediterranean depressions primarily influence rainfall (Figure 14, middle). In these locations, the precipitation maximum is recorded during the cold season (typically in November or December), and monthly precipitation can exceed 200 mm. The rainfall minimum commonly occurs in July or August. Negative scores are observed in most of the country, except for some mountainous regions.

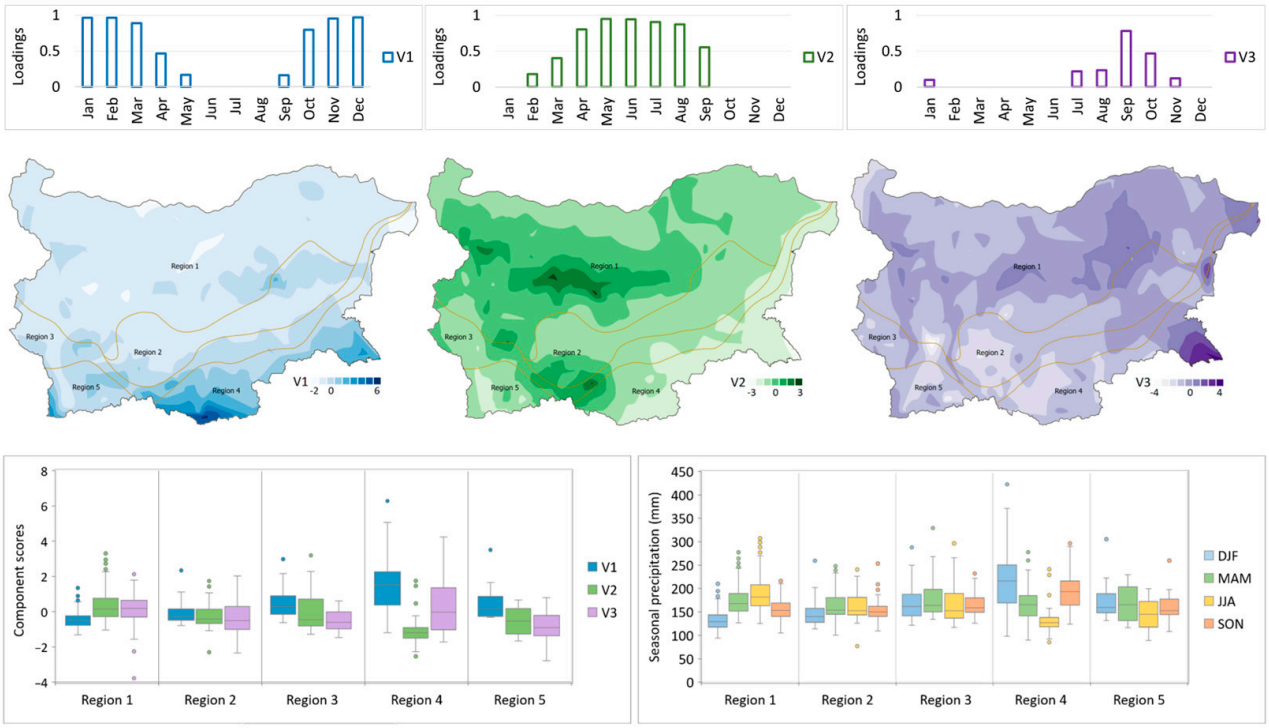


Figure 14. (**Top panel**): Component loadings. (**Middle panel**): Spatial patterns of component scores. (**Bottom panel**): Box plots of component scores (**left**) and modeled seasonal precipitation (**right**) by precipitation regions; V1 to V3 denote the varimax-rotated principal components.

Component V2, which accounts for 38% of the total variance, shows the highest loadings for rainfall in May and June (Figure 14, top). Higher scores are commonly found in the central and western mountainous areas, which are characterized by substantial monthly rainfall during the warm season (typically in May and June). Conversely, higher negative scores are observed primarily in the southernmost regions and the coastal zone, where summer rainfall is relatively smaller (Figure 14, middle). The analysis of synoptic conditions over the Balkan Peninsula during the warm season reveals that the summer circulation is dominated by the west-to-east transfer of Atlantic air masses in the system of anticyclones or high-pressure ridges. It is one of the primary factors controlling convective processes over a large part of the domain [62].

Component V3 (8% of the total variance) shows higher loadings for rainfall in September and October (Figure 14, top). The highest scores are associated with stations located mainly in the eastern part of the country, which experience significant rainfall peaks during autumn (Figure 14, middle). Stations in southeastern regions often record their maximum rainfall in October, when the northeastern anticyclones and active cyclogenesis in the Eastern Mediterranean trigger thunderstorms, sometimes causing considerable damage over the coastal zone and southeastern regions [62].

These findings are consistent with the outcomes of the T-mode factor analysis for the southern Balkans, conducted on the APHRODITE dataset by Lolis [26], which results in three main modes of spatial distribution of precipitation: “cold period mode” (November to March), “warm period mode” (April to August), and “autumn mode” (September to October).

The spatial patterns of component scores align with the existing division of Bulgaria into precipitation regions. Namely, component V1 shows higher scores in regions with a well-expressed Mediterranean climate influence (Regions 4 and 5), whereas component V2 shows higher scores in regions with continental climate influence (Regions 1 and 2).

The PC scores explain the contribution of individual components to the precipitation regime at each station, presented by climate normals. Depending on whether PC scores are positive or negative (especially in months when the individual PCs have the highest loadings), a given station will indicate values above or below the country average. More specifically, box plots of rotated PC scores by precipitation region (Figure 14, bottom left) reveal that the contribution of V1 is predominantly negative in Region 1. The contributions of V2 and V3 are mostly negative in Regions 4 and 5, respectively. Figure 14 (bottom right) shows the seasonal precipitation modeled by the varimax-rotated PCs. The results agree with the seasonal precipitation climatology in Bulgaria, as presented in a recent study [60]. Generally, three precipitation regimes are well distinguishable—continental, with a summer maximum and winter minimum (Region 1); Mediterranean, with a winter maximum and summer minimum (Region 4); and transitional, without clear seasonal peaks (Regions 2, 3, and 5). Regarding the transitional type, in Region 2, it is similar to a continental climate, with the lowest seasonal precipitation occurring in winter. In contrast, Region 5 exhibits a Mediterranean-like climate, characterized by a summer minimum.

Given that the intra-annual course of hazardous rainfall corresponds to the precipitation regimes in the country [61], we examined the link between circulation patterns associated with HREs and the precipitation regimes identified using PCA. Figure 15 illustrates the monthly CWT frequencies (in %) for the study period, averaged across stations with positive varimax scores for only one of the principal components: V1 (17 stations in Region 4, 3 in Region 2, and 7 each in Region 3 and 5), V2 (41 stations in Region 1 and 4 in Region 2), and V3 (38 stations in Region 1, 9 in Region 2, and 8 in Region 4).

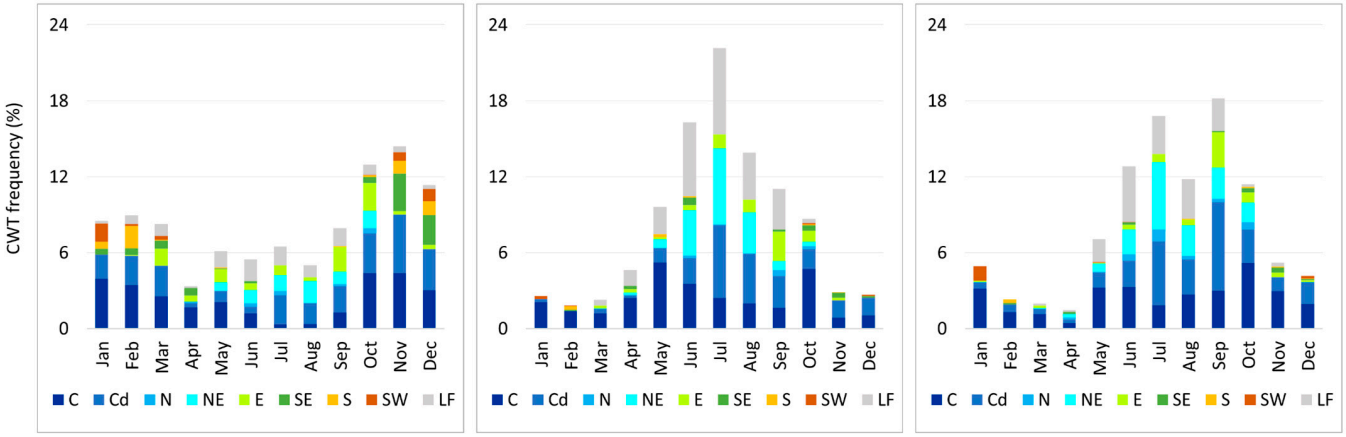


Figure 15. Monthly frequencies (in %) of CWTs linked to HREs for 1991–2020, averaged across stations with positive varimax scores for only one of the principal components: V1 (**left panel**), V2 (**middle panel**), and V3 (**right panel**).

Regarding the intra-annual distribution of CWTs associated with the V1 pattern, the overall occurrence of cyclonic types (C and Cd) is 54.1%, with an obvious summer minimum (Figure 15, left). The frequency of LF (10.3%) is comparable to the most frequent directional CWTs during the warm season, E (9.3%) and NE (7.1%). During the cold season, the most frequently occurring directional CWTs are SE (8.3%), S (4.7%), and SW (3.7%).

The overall occurrence of cyclonic types associated with the V2 pattern is 49%. LF (23.7%) is the second most frequent CWT. The most frequent warm season directional CWTs are NE (14.8%) and E (6.6%). The frequency of typical cold season directional CWTs is negligible (Figure 15, middle).

The distribution of CWTs associated with the V3 pattern is shown in Figure 15, right. The highest frequency occurs for cyclonic types (55.5%) and LF (15.6%). The most fre-

quent directional CWT in the warm season is NE (14.7%). Among the typical cold season directional CWTs, only the SW type exhibits some influence, at 1.2% in January.

The regionalization of precipitation regimes is based on k-means clustering of the rotated component scores, using the R package "NbClust". We identified seven zones with similar precipitation characteristics. The homogeneity of regions was assessed on the D1 dataset (see Appendix D for details).

The following brief description uses information from Table 3, which shows the averaged monthly and annual precipitation amounts by cluster, and from Figure 16, which illustrates the spatial distribution of clusters. The identified seven clusters (C1, C2,. . . , C7) reveal distinct annual precipitation patterns.

Table 3. Average monthly ("Jan" to "Dec") and annual ("Ann.") precipitation (unit: mm) by cluster, calculated on the D1 dataset; the seven clusters are labeled C1 to C7.

	Jan	Feb	Mar	Apr	May	Jun	Jul	Aug	Sep	Oct	Nov	Dec	Ann.
C1	51.8	50.0	61.4	68.1	97.8	96.1	84.9	59.0	67.2	65.8	50.2	58.1	810
C2	48.3	41.6	48.1	45.2	57.5	64.6	58.0	40.7	56.9	58.0	50.7	53.1	623
C3	80.2	64.6	66.6	49.1	44.1	48.6	41.5	35.2	66.6	103.0	83.9	84.1	768
C4	45.6	41.7	48.3	45.3	56.9	56.4	47.6	35.0	44.7	52.1	47.3	54.0	575
C5	68.0	66.0	75.9	69.6	94.1	98.8	76.4	55.6	55.7	61.0	68.7	89.2	879
C6	40.2	37.7	46.7	51.5	72.4	73.1	64.6	45.6	52.0	53.1	41.6	46.0	624
C7	85.6	78.3	76.5	59.1	67.2	59.1	44.3	29.5	48.7	79.5	89.0	104.6	822

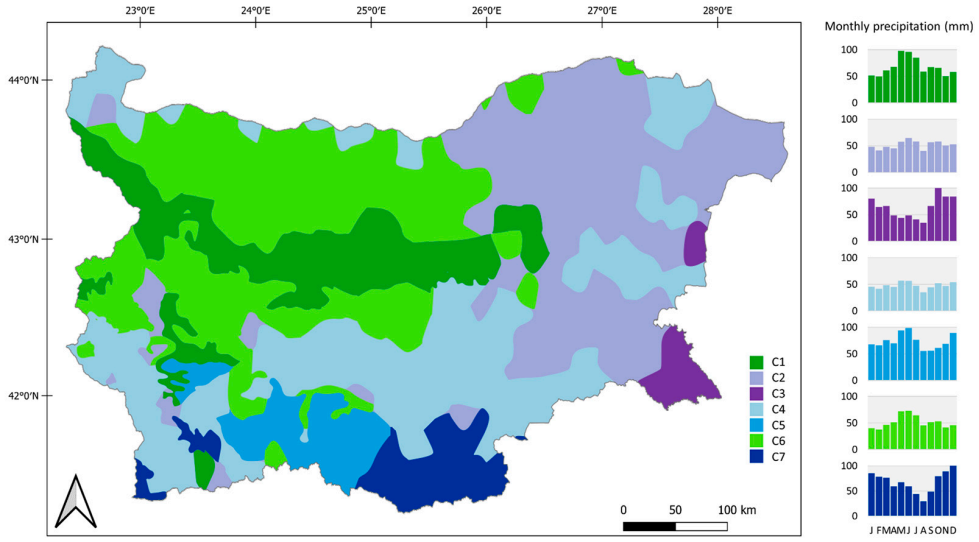


Figure 16. Regionalization of precipitation regimes obtained by applying k-means clustering on the scores of varimax-rotated PC; monthly precipitation by cluster is calculated on the D1 dataset.

Cluster C1 comprises 47 stations located in the mountainous and sub-mountainous areas of the central and western parts of the country. The annual precipitation is 810 mm, with a maximum in May or June. This cluster is primarily characterized by positive scores across all three components.

Cluster C2 includes 82 stations mainly located in the eastern part of the country. The annual precipitation is 623 mm. Monthly precipitation is almost uniformly distributed, with a weakly expressed maximum in June. Overall, this cluster features consistently positive V3 scores.

Cluster C3 comprises seven stations situated in the easternmost parts of the country. The maximum monthly rainfall typically occurs in October, and the annual precipitation is 768 mm. This cluster featured significantly positive V1 and V3 and negative V2 scores.

Cluster C4 includes 90 stations, mainly located along the Danube River and the larger river basins of the southern and eastern regions. The mean annual precipitation is the lowest, 575 mm. The distribution of monthly precipitation is almost uniform. This cluster primarily featured consistently negative V3 scores and negative or weakly expressed positive V1 and V2 scores.

Cluster C5 comprises 20 stations located in the middle- and high-altitude areas of Rila and the Western Rhodopes, exhibiting an orographically influenced precipitation regime. The mean annual precipitation is the highest, 879 mm, with a maximum in June and a secondary maximum in December. This cluster featured higher positive V1 and V2 scores and negative V3 scores.

Cluster C6 comprises 93 stations, mainly located in the western and central parts of the Danube Plain, as well as stations situated in the high valleys and low-altitude areas south of the Balkan Mountains. The mean annual precipitation is 624 mm. The precipitation regime is comparable to Cluster 1, but orographic influence is rather low-expressed. This cluster is characterized mainly by positive V2 and negative V1 scores.

Cluster C7 includes 16 stations, located mostly in the Eastern Rhodopes, with a Mediterranean-like precipitation regime, but without dry months. The mean annual precipitation is the second highest, 822 mm, with a maximum in December. This cluster featured significant positive V1 scores.

3.3. Regionalization of Torrential Rainfall

Following the approach used in the analysis of precipitation regimes, we sought a historical regionalization of HREs that can be used in comparison with the results from PCA and CA. Unfortunately, no relevant studies have been conducted on HRE spatial patterns in Bulgaria. Therefore, we decided to use the map of the annual frequency of ORWs and RDWs for the period 2011–2020 by district (Figure 13, top right), considering that each issued warning is the result of expert judgment. This regionalization offers several advantages: (1) it is based on a relatively large dataset of daily data; (2) the period 2011–2020 represents the most recent decade within the entire study period; (3) the resulting map can be considered as a vulnerability map to HREs for the entire study period, as there were no substantial changes in the annual frequency of ORW and RDW events during the considered period.

We have conducted T-mode PCA on the D3 dataset to join days with similar spatial patterns (see Appendix E for details). Next, we performed a k-means clustering on varimax-rotated PC scores using the R package "NbClust".

The nine identified clusters (CL1, CL2,. . . , CL9) present the primary patterns of torrential rainfall. The brief description presented hereafter uses information from Table 4, which presents the CWT contribution to torrential rainfall for each cluster (in %). Also, it refers to Figure 17, which shows the spatial distribution of clusters.

Cluster CL1 includes 35 stations situated in northwestern Bulgaria. The contribution of torrential rainfall to the annual precipitation is among the lowest (11.4 mm), with the most significant proportion of LF (35.4%).

Cluster CL2 comprises 18 stations in southeastern Bulgaria, with the second-highest contribution to annual precipitation (35.7 mm). The proportion of easterlies (35.5%) and cyclonic easterlies (26.6%) is the most significant, while that of LF (5.9%) is one of the lowest among the clusters.

Cluster CL3 comprises stations located in northeastern Bulgaria, including the coastal zone. The contribution to annual precipitation is 16.2 mm, with larger proportions of cyclonic type, easterlies, and cyclonic easterlies (24.4% to 28.3%).

Table 4. CWT contribution (in %) to torrential rainfall by cluster; the nine clusters are noted as CL1 to CL9.

	C	CN	CNE	CE	CSE	CS	CSW	CW	CNW	A*	N	NE	E	SE	S	SW	W	NW	LF
CL1	16.2	0.7	22.0	2.4	3.9	0.0	0.0	0.0	0.0	0.0	0.0	9.8	9.9	0.0	0.0	0.0	0.0	0.0	35.4
CL2	19.1	0.4	2.7	19.4	4.5	0.0	3.2	0.0	0.0	1.9	3.8	12.6	20.9	2.0	0.0	3.0	0.6	0.0	5.9
CL3	28.3	4.3	7.7	18.7	1.8	0.0	0.0	0.0	0.9	1.8	0.6	16.6	7.3	0.5	0.0	0.0	0.0	0.0	11.4
CL4	17.8	0.8	22.9	4.5	0.0	0.0	0.0	0.0	0.0	1.4	1.3	9.2	10.2	5.7	0.6	0.0	0.0	0.0	25.5
CL5	28.6	0.0	4.5	11.6	12.2	5.9	5.9	0.0	0.0	0.7	0.0	3.6	9.7	2.4	5.1	4.0	0.0	0.0	5.8
CL6	25.8	1.2	12.3	5.6	17.3	0.0	0.0	0.0	1.1	0.0	1.2	9.7	0.0	0.0	0.9	0.0	0.0	0.0	24.8
CL7	21.7	8.6	10.2	4.4	2.7	0.9	2.5	0.0	1.4	0.2	1.2	18.4	5.2	3.6	1.9	0.7	0.0	0.0	16.3
CL8	28.0	7.5	14.8	5.7	2.5	0.3	0.0	0.0	0.7	0.7	4.2	17.2	9.3	0.3	0.0	0.4	0.0	0.0	8.4
CL9	29.7	0.0	0.5	4.5	5.7	8.8	12.3	0.0	0.0	0.0	0.0	1.0	7.0	7.8	6.2	11.9	0.0	0.0	4.5

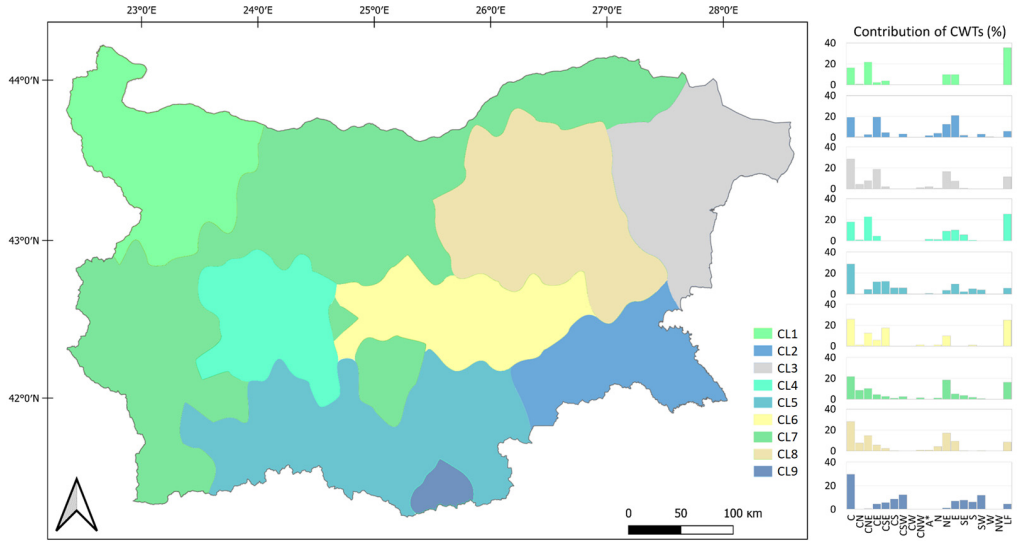


Figure 17. Regionalization of torrential rainfall in the period 1991–2020; charts represent the CWT contribution to torrential rainfall (in %) by cluster.

Cluster CL4 includes 21 stations, mainly located in the sub-mountain areas of the central western part of the country. The contribution to annual precipitation is 15.7 mm. Both the CNE (22.9%) and LF (25.5%) types have the highest contribution among clusters.

Cluster CL5 comprises 47 stations, located mainly in the Rhodopes and adjacent foothills. The contribution to annual precipitation is 23.2 mm, dominated by the cyclonic type (28.6%) and cyclonic easterlies (28.3%).

Cluster CL6 comprises 23 stations, mainly located in the Upper Thracian Lowland and valleys south of the Balkan Mountains. The contribution to annual precipitation is 11.1 mm, with almost equal proportions of C (25.8%) and LF (24.8%) types and the highest contribution of cyclonic easterlies (35.3%).

Cluster CL7 includes 118 stations across the country, mainly in the southwestern and central northern parts. The contribution to annual precipitation is the lowest (9.1 mm), but the proportions of CN (8.6%) and NE (18.4%) types are the highest among the clusters.

Cluster CL8 includes 40 stations in the northeastern part of the country. The contribution to annual precipitation is 17.5 mm, with significant proportions of cyclonic types (28%), as well as easterlies (26.8%) and cyclonic easterlies (23.1%).

Cluster CL9 includes three stations in the central southernmost part of the country. The contribution to annual precipitation is the highest (147.9 mm), with the highest proportion of cyclonic types (29.7%) and CWTs with southerly advection (up to 12.3% for CSW type) among clusters. The LF (4.5%) contribution is the lowest among clusters.

To test the suitability of the proposed regionalization, we have calculated (1) the weighted contribution of clusters to torrential rainfall by district, and (2) the average torrential rainfall by district using station data. Figure 18 illustrates the good visual agreement between the measures.

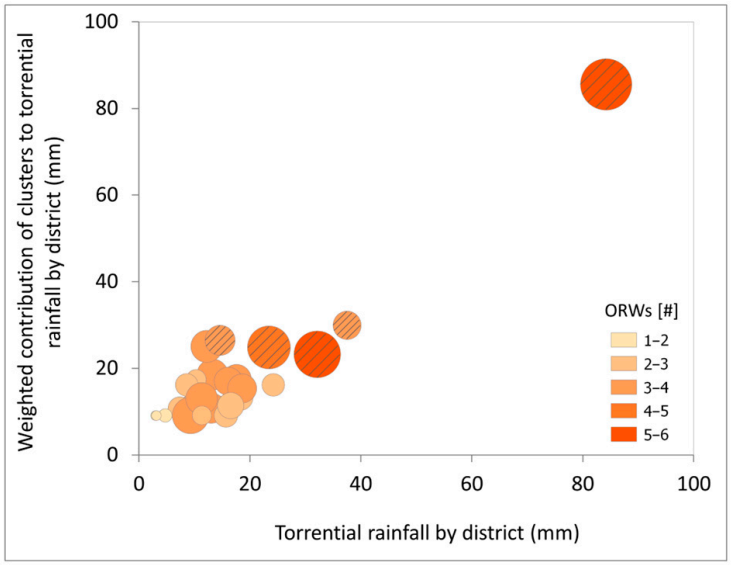


Figure 18. Bubble diagram comparing the weighted contribution of clusters to the torrential rainfall by district with the calculated torrential rainfall from station data by district; the size of bubbles is proportional to the average annual number of ORWs; bubbles are colored and dashed, following the visualization scheme of Figure 16, right.

The calculated pairwise Spearman correlation coefficients confirm the good agreement between the measures (0.670) and between the measures and the average annual number of ORWs (0.584 and 0.593, respectively).

The contribution of CWTs to torrential rainfall by clusters represents unique combinations. Our findings indicate that torrential rains are primarily associated with low-pressure systems and air flows from the east and northeast, as well as with low-flow circulation. The conducted principal component analysis reveals distinct spatial patterns in the component scores, which may be associated with different circulation conditions influenced by topography and proximity to the Black and Mediterranean Seas (see Figure A4 in Appendix E). We will elaborate on these aspects in a future study that includes relevant case studies of torrential rainfall.

We intend to continue this research by emphasizing the potential application of the proposed regionalization of torrential rainfall within statistical downscaling models and regional frequency analysis. Regionalization schemes based on climatological criteria and large-scale atmospheric circulation have been effectively applied in climate change and engineering studies (e.g., [84–86]). Our objective is to apply censored quantile regression models across a range of quantiles to capture the full spectrum of rainfall intensities. The predictors will include finite Fourier series based on the day of the year, together with daily NCEP–NCAR reanalysis fields of sea level pressure, 700 hPa specific humidity, and 500 hPa geopotential height. These predictors will be used for the same period as the precipitation observations.

We anticipate that this approach will provide a suitable framework to achieve two main objectives:

(1) To evaluate changes in rainfall patterns under future climate scenarios using CMIP6 projections, specifically focusing on the high-impact clusters.

(2) To conduct a regional frequency analysis of precipitation that allows for a significant reduction in errors in quantile estimations.

4. Conclusions

The main objectives of this study were (1) to characterize precipitation regimes in Bulgaria under current climatic conditions; (2) to identify the relationships between precipitation regimes, hazardous precipitation events, and atmospheric circulation over the country; and (3) to propose an appropriate regionalization of torrential rainfall.

To achieve these objectives, we used three independent datasets corresponding to the respective aims: (1) daily precipitation data from the NIMH meteorological archive for the period 1991–2020; (2) mean daily sea level pressure data from the NCEP-NCAR reanalysis for the same period; and (3) data from the MA archive of heavy precipitation warnings covering 2011–2020.

The methodology used to establish precipitation regimes and torrential rainfall patterns is based on T-mode PCA with varimax rotation, followed by k-means clustering of the rotated components, applied to the relevant datasets (D1 and D3).

Our findings can be summarized as follows:

- The seasonal precipitation patterns revealed through PCA and the spatial distribution of component scores are consistent with precipitation regimes and the existing division of Bulgaria into precipitation regions. The seven identified clusters exhibit distinct annual precipitation patterns.
- Generally, HREs under cyclonic circulation, several directional, and low-flow types make the most significant contribution to annual precipitation. Among the directional CWTs, the most frequent during winter are southerlies (SW, S, and SE), while easterlies (NE, E, and SE) are the most frequent during spring and autumn.
- The main patterns of torrential rainfall identified through PCA account for approximately 77% of the total variance. The proposed regionalization consists of nine clusters, each with a unique combination of CWTs that contribute to torrential rain events. Our findings indicate that torrential rains are primarily associated with low-pressure systems, easterly and northeasterly flows, and low-flow circulation (weak-gradient pressure fields). There is a good agreement between the annual number of ORWs and the contribution of clusters to torrential rainfall by district.

The study provides new insights into the main characteristics of circulation weather types and their linkages with precipitation patterns and hazardous rainfall events, based entirely on objective methods and three independent data sources. Furthermore, data on meteorological alerts for hazardous rainfall have been used for the first time as a reference in the regionalization of hazardous rainfall. To our knowledge, this approach is new to Bulgaria.

The proposed regionalization offers a physically meaningful basis for evaluating region-specific precipitation forecasting, particularly for extreme events, delineating regions with distinct circulation conditions for triggering torrential rainfall. In addition, the identified torrential rainfall patterns, especially the high-impact ones, can help assess potential future shifts in the behavior of extreme events using CMIP6 projections. Finally, regionalization can support flood hazard zoning by improving estimates of precipitation quantiles, accounting for region-specific characteristics of extreme rainfall.

In this way, the study extends beyond its climatological perspective and can contribute to the improved forecasting and assessment of climate change impacts.

Author Contributions: Conceptualization, K.M. and L.B.; methodology, K.M.; software, K.M., N.N. (Neyko Neykov), and N.N. (Nadya Neykova); validation, K.M. and N.N. (Neyko Neykov); formal analysis, L.B., A.S., and N.N. (Nadya Neykova); data curation, L.B. and A.S.; writing—original draft preparation, K.M.; writing—review and editing, A.S., N.N. (Neyko Neykov), and L.B.; visualization, K.M. and N.N. (Neyko Neykov). All authors have read and agreed to the published version of the manuscript.

Funding: This research received no external funding.

Data Availability Statement: The datasets presented in this article are not readily available because the data are part of an ongoing study. Requests to access the datasets should be directed to the corresponding author.

Acknowledgments: We would like to thank NOAA PSL, Boulder, CO, USA, for free data provided from their website at https://psl.noaa.gov (accessed on April 2 2025).

Conflicts of Interest: The authors declare no conflicts of interest.

Abbreviations

The following abbreviations are used in this manuscript:

Ad	Group of hybrid anticyclonic CWTs
APHRODITE	Asian Precipitation—Highly Resolved Observational Data Integration Towards Evaluation
Cd	Group of hybrid cyclonic CWTs
CWT	Circulation weather type
ERA^5	The fifth-generation atmospheric reanalysis of the European Centre for Medium-Range Weather Forecasts (ECMWF)
HRE	Hazardous rainfall event
JC	Jenkinson–Collison's automated approach to classify atmospheric circulation patterns based on sea level pressure
MA	MeteoAlarm—European Early Warning Dissemination System
MSLP	Mean sea level pressure
NCAR	The US National Center for Atmospheric Research
NCEP	The US National Centers for Environmental Prediction
NIMH	National Institute of Meteorology and Hydrology, Bulgaria
ORW	Orange code MA warning
RDW	Red code MA warning
WMO	World Meteorological Organization
YLW	Yellow code MA warning

Appendix A

Table A1. Key information for 119 synoptic and climatic stations from the NIMH meteorological network used in the study; "Region" denotes the regions from the existing regionalization of precipitation in Bulgaria [61].

Station Name	District	Latitude (N)	Longitude (E)	Altitude (m)	Type	Region
Ahtopol	Burgas	27.9523	42.0841	27	synoptic	Region 4
Alfatar	Silistra	27.2884	43.9455	163	climatic	Region 1
Asenovgrad	Plovdiv	24.8768	42.0108	233	climatic	Region 2
Bankya	Sofia City	23.1508	42.7047	652	climatic	Region 1
Bansko	Blagoevgrad	23.4931	41.8397	920	climatic	Region 5
Bazovets	Montana	23.5519	43.6288	142	climatic	Region 1

Table A1. *Cont.*

Station Name	District	Latitude (N)	Longitude (E)	Altitude (m)	Type	Region
Belogradchik	Vidin	22.6894	43.6279	542	climatic	Region 1
Blagoevgrad	Blagoevgrad	23.0981	42.0019	424	synoptic	Region 3
Borima	Lovech	24.5753	42.9745	476	climatic	Region 1
Borovets	Sofia	23.5967	42.2728	1257	climatic	Region 1
Botevgrad	Sofia	23.8001	42.9002	350	climatic	Region 1
Bozhurishte	Sofia	23.2069	42.7619	562	climatic	Region 1
Brashlen	Ruse	26.3634	43.9923	34	climatic	Region 1
Burgas	Burgas	27.4827	42.4977	22	synoptic	Region 4
Chepelare	Smolyan	24.6882	41.7182	1100	climatic	Region 2
Chirpan	Stara Zagora	25.2825	42.2145	162	synoptic	Region 2
Dalgopol	Varna	27.3473	43.0508	38	climatic	Region 2
Dermantsi	Lovech	24.2831	43.1559	199	climatic	Region 1
Devin	Smolyan	24.4262	41.7218	711	climatic	Region 2
Divlya	Pernik	22.6881	42.5797	742	climatic	Region 1
Dobrich	Dobrich	27.8361	43.5850	214	synoptic	Region 1
Dr. Yosifovo	Montana	23.1425	43.5018	208	climatic	Region 1
Dragoman	Sofia	22.9333	42.9317	736	synoptic	Region 1
Dupnitsa	Kyustendil	23.1185	42.2650	472	climatic	Region 3
Dve Mogili	Ruse	25.8739	43.5899	237	climatic	Region 1
Dzhebel	Kardzhali	25.2958	41.4978	324	climatic	Region 4
Elena	Veliko Tarnovo	25.8747	42.9231	330	climatic	Region 1
Elhovo	Yambol	26.5830	42.1766	145	synoptic	Region 3
Emine	Burgas	27.8998	42.7012	55	synoptic	Region 2
Gabrovo	Gabrovo	25.3257	42.8646	454	climatic	Region 1
General Toshevo	Dobrich	28.0309	43.6543	237	climatic	Region 1
Glavinitsa	Silistra	26.8390	43.9154	150	climatic	Region 1
Goren Chiflik	Varna	27.6297	43.0094	29	climatic	Region 3
Gramada	Vidin	22.6616	43.8277	243	climatic	Region 1
Haskovo	Haskovo	25.5414	41.9279	237	synoptic	Region 4
Hisarya	Plovdiv	24.7179	42.4857	323	climatic	Region 1
Hvoyna	Smolyan	24.6873	41.8714	728	climatic	Region 2
Ihtiman	Sofia	23.8196	42.4381	637	climatic	Region 1
Iskrets	Sofia	23.2758	42.9817	565	climatic	Region 1
Isperih	Razgrad	26.8262	43.7125	265	climatic	Region 1
Ivaylo	Pazardzhik	24.3401	42.2311	217	synoptic	Region 2
Ivaylovgrad	Kardzhali	26.1211	41.5286	202	climatic	Region 4
Kaliakra	Dobrich	28.4656	43.3634	59	synoptic	Region 4
Kardzhali	Kardzhali	25.3854	41.6468	333	synoptic	Region 4
Karlovo	Plovdiv	24.7994	42.6466	484	climatic	Region 1
Karnobat	Burgas	26.9848	42.6558	195	synoptic	Region 2
Kazanlak	Stara Zagora	25.3878	42.6357	397	synoptic	Region 1
Knezha	Pleven	24.0696	43.4801	127	synoptic	Region 1
Koprivshtitsa	Sofia	24.3540	42.6406	1041	climatic	Region 1
Kostenets	Sofia	23.8525	42.3072	540	climatic	Region 1
Kotel	Sliven	26.4414	42.8887	475	climatic	Region 2
Kresna	Blagoevgrad	23.1628	41.7222	177	climatic	Region 5
Krumovgrad	Kardzhali	25.6600	41.4654	238	climatic	Region 4
Krushari	Dobrich	27.7537	43.8081	215	climatic	Region 1
Kyustendil	Kyustendil	22.7231	42.2819	520	synoptic	Region 3
Lom	Montana	23.2229	43.8307	36	synoptic	Region 1

Table A1. *Cont.*

Station Name	District	Latitude (N)	Longitude (E)	Altitude (m)	Type	Region
Lovech	Lovech	24.7007	43.1632	215	synoptic	Region 1
Lyulyakovo	Burgas	27.0844	42.8744	214	climatic	Region 2
Malko Tarnovo	Burgas	27.5289	41.9764	364	climatic	Region 4
Montana	Montana	23.2158	43.3890	203	synoptic	Region 1
Nikolaevo	Pleven	24.6006	43.2594	289	climatic	Region 1
Novachene	Pleven	24.9234	43.5535	45	climatic	Region 1
Novo Selo	Vidin	22.7847	44.1648	40	synoptic	Region 1
Obraztsov Chiflik	Ruse	26.0411	43.8078	155	climatic	Region 1
Omurtag	Targovishte	26.4219	43.1049	533	climatic	Region 1
Oryahovo	Vratsa	23.9629	43.7409	31	synoptic	Region 1
p. Botev	Plovdiv	24.9174	42.7171	2376	synoptic	Region 1
p. Cherni Vrah	Sofia City	23.2785	42.5638	2286	synoptic	Region 1
p. Murgash	Sofia City	23.6689	42.8329	1687	synoptic	Region 1
p. Musala	Sofia	23.5851	42.1793	2925	synoptic	Region 1
Panagyurishte	Pazardzhik	24.1742	42.5137	562	climatic	Region 1
Parvomay	Blagoevgrad	23.1408	41.4044	134	climatic	Region 5
Pavlikeni	Veliko Tarnovo	25.3252	43.2342	140	climatic	Region 1
Pernik	Pernik	23.0206	42.6014	712	climatic	Region 1
Peshtera	Pazardzhik	24.3044	42.0337	456	climatic	Region 2
Pleven	Pleven	24.6063	43.4074	160	synoptic	Region 1
Plovdiv	Plovdiv	24.8025	42.1343	154	synoptic	Region 2
Raikovo	Smolyan	24.7135	41.5739	906	climatic	Region 3
Razgrad	Razgrad	26.5077	43.5662	343	synoptic	Region 1
Rezovo	Burgas	28.0288	41.9841	19	climatic	Region 4
Rila	Kyustendil	23.1308	42.1253	528	climatic	Region 3
Rozhen	Smolyan	24.7391	41.6946	1771	synoptic	Region 3
Ruse 2	Ruse	25.9700	43.8532	46	climatic	Region 1
Ruse 1	Ruse	25.9450	43.8402	46	synoptic	Region 1
Sadievo	Sliven	26.0778	42.5333	163	climatic	Region 2
Sadovo	Plovdiv	24.9369	42.1289	153	climatic	Region 2
Samokov	Sofia	23.5653	42.3392	946	climatic	Region 1
Samuil	Razgrad	26.7500	43.5167	474	climatic	Region 1
Sandanski	Blagoevgrad	23.2672	41.5500	206	synoptic	Region 5
Sevlievo	Gabrovo	25.1151	43.0256	197	climatic	Region 1
Shabla	Dobrich	28.6054	43.5389	5	synoptic	Region 4
Shumen	Shumen	26.9440	43.2796	217	synoptic	Region 2
Silistra	Silistra	27.2661	44.1239	16	synoptic	Region 1
Slavyanovo	Targovishte	26.1743	43.2921	334	climatic	Region 1
Sliven	Sliven	26.3399	42.6777	267	synoptic	Region 2
Sofia	Sofia City	23.3829	42.6538	586	synoptic	Region 1
Somovit	Pleven	24.7852	43.6882	55	climatic	Region 1
Sredets	Burgas	27.1763	42.3473	25	climatic	Region 4
Stara Zagora	Stara Zagora	25.6470	42.3868	162	synoptic	Region 2
Staro Oryahovo	Varna	27.7998	42.9896	14	climatic	Region 4
Sungurlare	Burgas	26.7670	42.7625	199	climatic	Region 2
Suvorovo	Varna	27.5914	43.3306	173	climatic	Region 1
Svishtov	Veliko Tarnovo	25.3461	43.6226	33	synoptic	Region 1
Targovishte	Targovishte	26.5859	43.2362	225	climatic	Region 1
Teteven	Lovech	24.2658	42.9158	422	climatic	Region 1
Topolovgrad	Haskovo	26.3264	42.0903	304	climatic	Region 3
Tran	Pernik	22.6578	42.8331	747	climatic	Region 1

Table A1. *Cont.*

Station Name	District	Latitude (N)	Longitude (E)	Altitude (m)	Type	Region
Troyan	Lovech	24.7126	42.9008	391	climatic	Region 1
Tsarev Brod	Shumen	27.0124	43.3244	234	climatic	Region 1
Tvarditsa	Sliven	25.8924	42.6998	375	climatic	Region 1
Varna	Varna	27.9523	43.2125	39	synoptic	Region 4
Varshets	Montana	23.2935	43.1925	412	climatic	Region 1
Veliko Tarnovo	Veliko Tarnovo	25.6183	43.0733	194	synoptic	Region 1
Velingrad	Pazardzhik	23.9888	42.0120	734	climatic	Region 1
Vidin	Vidin	22.8525	43.9943	34	synoptic	Region 1
Vratsa	Vratsa	23.5292	43.2312	311	synoptic	Region 1
Yambol	Yambol	26.5315	42.4751	132	climatic	Region 2
Zlatitsa	Sofia	24.1452	42.7109	690	climatic	Region 1
Zlatograd	Smolyan	25.0871	41.3868	449	climatic	Region 4

Appendix B

The majority of stations in the NIMH network conduct only daily climatological precipitation observations at 7:00 h (local time). As a result, the time series consists of 24 h precipitation totals from 7:00 h on the previous day to 7:00 h on the current day. Hence, an important source of uncertainty arose when aligning daily CWTs with HREs, as daily MSLP data are based on NCEP-NCAR reanalysis outputs at 00:00, 06:00, 12:00, and 18:00 UTC [49]. To evaluate this uncertainty, we conducted an additional analysis of archive data on the type and duration of heavy precipitation recorded at synoptic stations during the period 1991–2020.

There are two main approaches to the temporal alignment of daily climatological observations: simple one-day backshifting and hourly shifting after disaggregating daily precipitation [87,88]. Since research reported some drawbacks of using disaggregation (an increase in the frequency of events, along with a decrease in the number of extremes and average intensity), we focused our analysis on assessing the suitability of the one-day backshift method, specifically, on the frequency of cases when precipitation was registered mostly between 00:00 and 07:00 h. In these cases, applying a one-day backshift could increase the uncertainty in determining daily CWTs associated with heavy rainfall events. Considering that heavy and torrential rains generally occur on a small spatial scale and over a short timespan (less than a few hours) [62], we analyzed sub-daily rainfall occurrences at synoptic stations across the country, corresponding to each HRE and registered as climatological observations in at least three meteorological stations. This subsetting comprised all events, excluding highly localized and specific situations (a total of 1035 days). The results show that, in approximately 10% of events, precipitation mainly occurred between 00:00 and 07:00 h; in 4.3% of them, the backshift led to a substantial change in CWTs (e.g., from cyclonic to low-flow or from directional to anticyclonic). Nevertheless, for 80–90% of events, the one-day backshift approach has improved the alignment with CWTs and MA warnings.

Appendix C

Daily circulation affecting a given area is characterized by the set of indices associated with the direction and vorticity of geostrophic flow: southerly flow (SF), westerly flow (WF), total flow (F), southerly shear vorticity (ZS), westerly shear vorticity (ZW), and total shear vorticity (Z). These indices are computed using daily MSLP values obtained for the

16 grid points (p_1–p_{16}) shown in Figure A1, using the following expressions (ψ is the latitude of the central point):

$$SF = A[0.25(p_5 + 2p_9 + p_{13}) - 0.25(p_4 + 2p_8 + p_{12})], \quad A = 1/\cos(\psi) \tag{A1}$$

$$WF = [0.5(p_{12} + p_{13}) - 0.5(p_4 + p_5)] \tag{A2}$$

$$ZS = B[0.25(p_6 + 2p_{10} + p_{14}) - 0.25(p_5 + 2p_9 + p_{13}) - 0.25(p_4 + 2p_8 + p_{12}) + 0.25(p_3 + 2p_7 + p_{11})], \quad B = \sin(\psi)/\sin(\psi - 5) \tag{A3}$$

$$ZW = C[0.5\,(p_{15} + p_{16}) - 0.5\,(p_8 + p_9)] - D[0.5(p_8 + p_9) - 0.5(p_1 + p_2)], \quad C = \sin(\psi)/\sin(\psi + 5),\ D = 1/2(\cos^2(\psi)) \tag{A4}$$

$$F = (SF^2 + WF^2)^{1/2} \tag{A5}$$

$$Z = ZS + ZW \tag{A6}$$

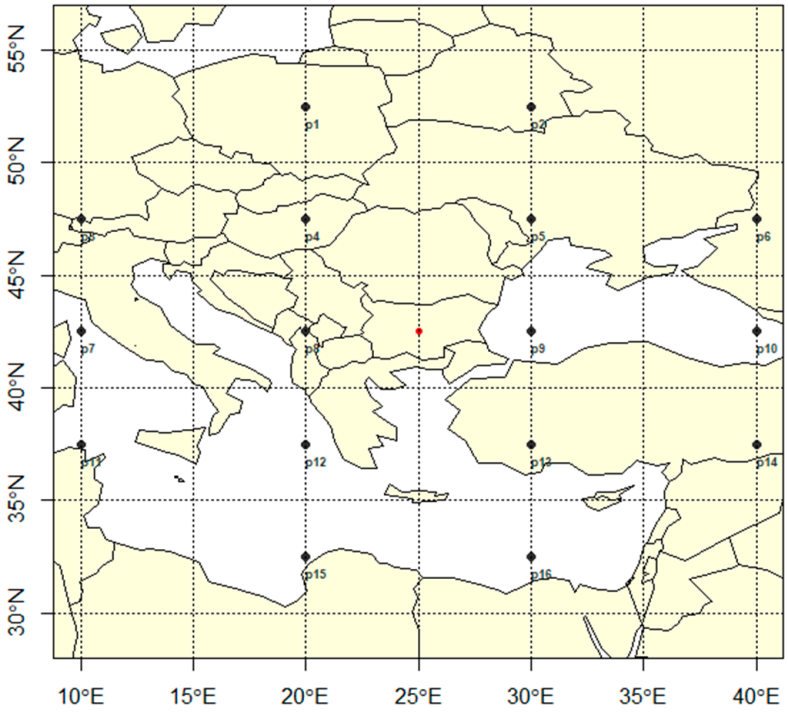


Figure A1. The distribution of the 16 grid points around a central point (in red), as generated by the R package "jcext".

Appendix D

We have conducted PCA in T-mode on the D1 dataset to identify general patterns in precipitation seasonality. After data standardization, the Kaiser–Meyer–Olkin measure of sampling adequacy (MSA) [89] is computed. The overall MSA is 0.87, with values for the individual variables ranging from 0.82 (December) to 0.93 (August), which allows us to conduct PCA. Based on the Kaiser criterion, with a weak constraint of 0.7 rather than 1.0 [90], three PCs (PC1, PC2, PC3) were extracted, accounting for approximately 91% of the total variance (Table A2). Scatterplots of identified PCs (Figure A2a,c,d) reveal that several variables load significantly on more than one component. The score plot in Figure A2b shows fuzzy clustering by region, although Region 1 and Region 4 are relatively better distinguishable.

Table A2. Proportion of variance of the first three principal components.

Component	1	2	3
Rotated: V	0.45	0.38	0.08
Unrotated: PC	0.53	0.32	0.06

Figure A3 (left column) illustrates the spatial distribution of PC scores. Varimax rotation has been applied to the principal components to achieve more stable patterns and maintain the orthogonality [91]. The obtained PCs (V1 to V3) explain the same total variance but with different proportions of variance compared to the unrotated PCs (Table A2). The orthogonally rotated PCs enable a better interpretation of the PCA results (Figure A3, right column). Their loadings exhibit a strong relationship with the intra-annual precipitation cycle across different climates (Figure A3, charts).

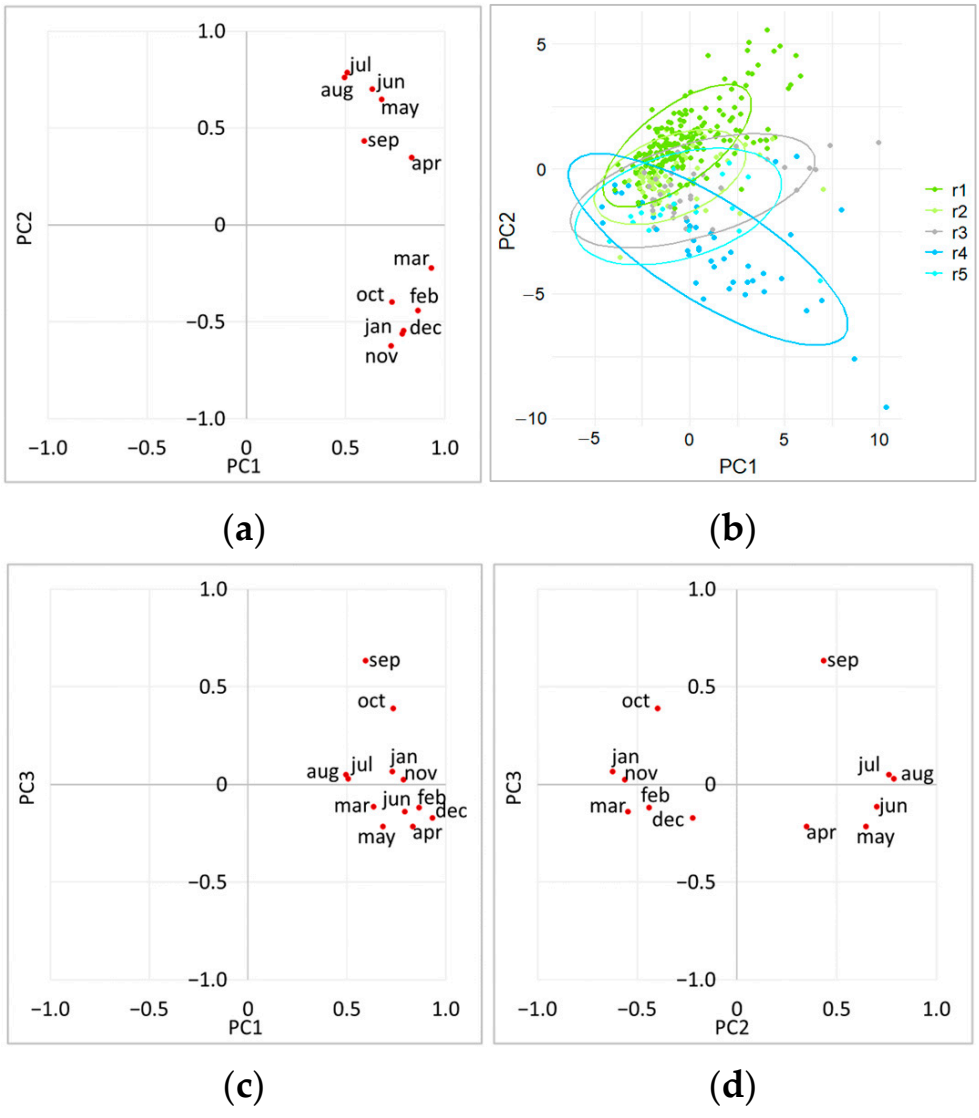


Figure A2. Scatterplots of loadings (**a**,**c**,**d**) and scores (**b**) of unrotated PCs; the regions shown in Figure 2 (bottom right panel) are labeled r1 to r5.

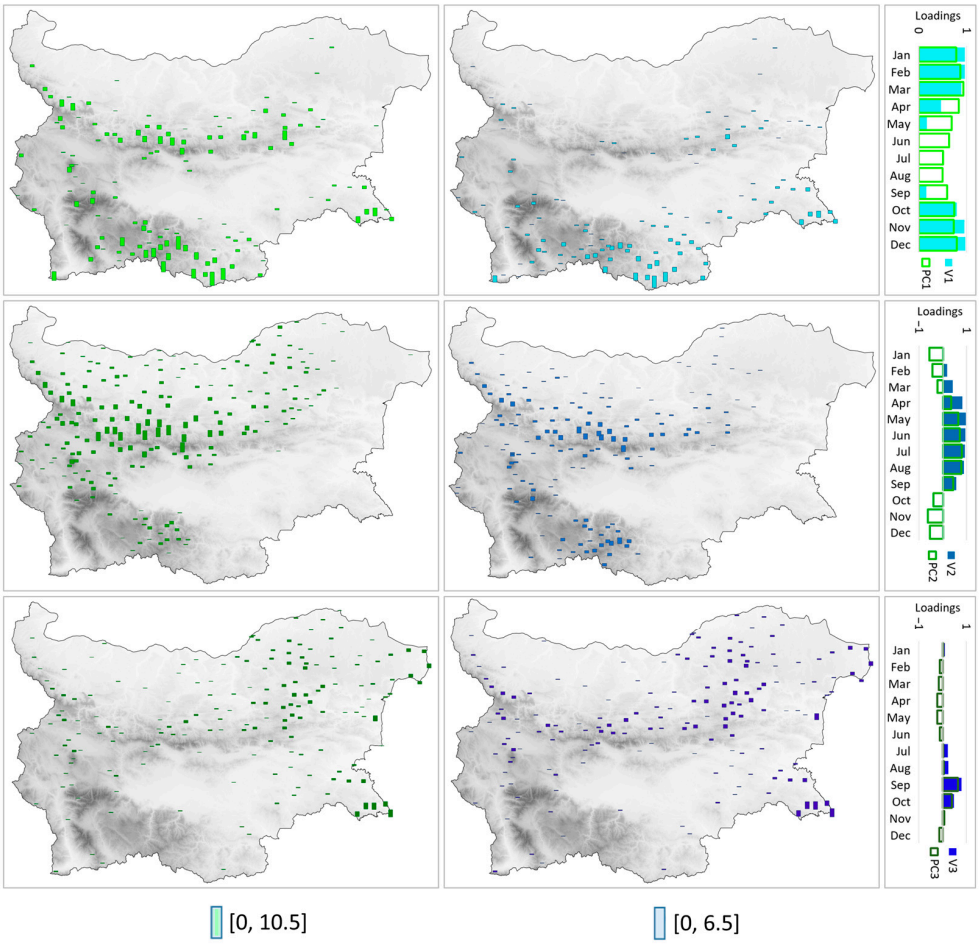


Figure A3. Regionalization of precipitation regimes by scores of unrotated (**left column**) principal components (PC1, PC2, PC3) and varimax-rotated components (**right column**)—V1, V2, V3; the negative scores are not visualized; charts show the eigenvector loadings.

The homogeneity of regions was assessed on the D1 dataset using the coefficient of variation by month (CVm) and the average within-group Pearson pairwise correlation (Ra) [77].

Cluster C1: The CV_m values vary between 0.08 (September) and 0.19 (January and November). The group homogeneity is high (Ra = 0.834), and 91% of the correlation coefficients exceed 0.6.

Cluster C2: CV_m ranges between 0.1 (September) and 0.2 (August). The group homogeneity is relatively low (R_a = 0.609), with 60% of the correlation coefficients exceeding 0.6.

Cluster C3: CV_m ranges between 0.12 (April and September) and 0.27 (May). The group homogeneity is the highest (R_a = 0.995), and 100% of correlation coefficients exceed 0.8.

Cluster C4: The CV_m values range from 0.1 (September) to 0.18 (February). The group homogeneity is low (R_a = 0.579), although the number of negative correlations is small, and 56% of the values fall within the range (0.6, 1.0).

Cluster C5: CV_m ranges from 0.12 (May and September) to 0.25 (November). The group homogeneity is relatively high (R_a = 0.778), and 81% of correlation coefficients exceed 0.6.

Cluster C6: CV_m ranges from 0.07 (September) to 0.14 (August and December). The group homogeneity is high (R_a = 0.884), and almost 100% of correlation coefficients fall within the range of 0.6 to 1.0.

Cluster C7: The CV_m values vary from 0.12 (April, May, and September) to 0.3 (November). The group homogeneity is high (R_a = 0.889), and 100% of correlation coefficients exceed 0.6.

Appendix E

Conducting T-mode PCA on the D3 dataset, we aim to join days with similar spatial patterns, regardless of the precipitation amounts across stations. After data standardization, the Kaiser–Meyer–Olkin measure of sampling adequacy is computed. The overall MSA is 0.86, with only three individual MSA values closer to the 0.5 critical value, which allows us to conduct PCA. Based on the Kaiser criterion [90], 30 PCs are extracted, accounting for approximately 77% of the total variance. The spatial patterns of the varimax-rotated PC scores are shown in Figure A4.

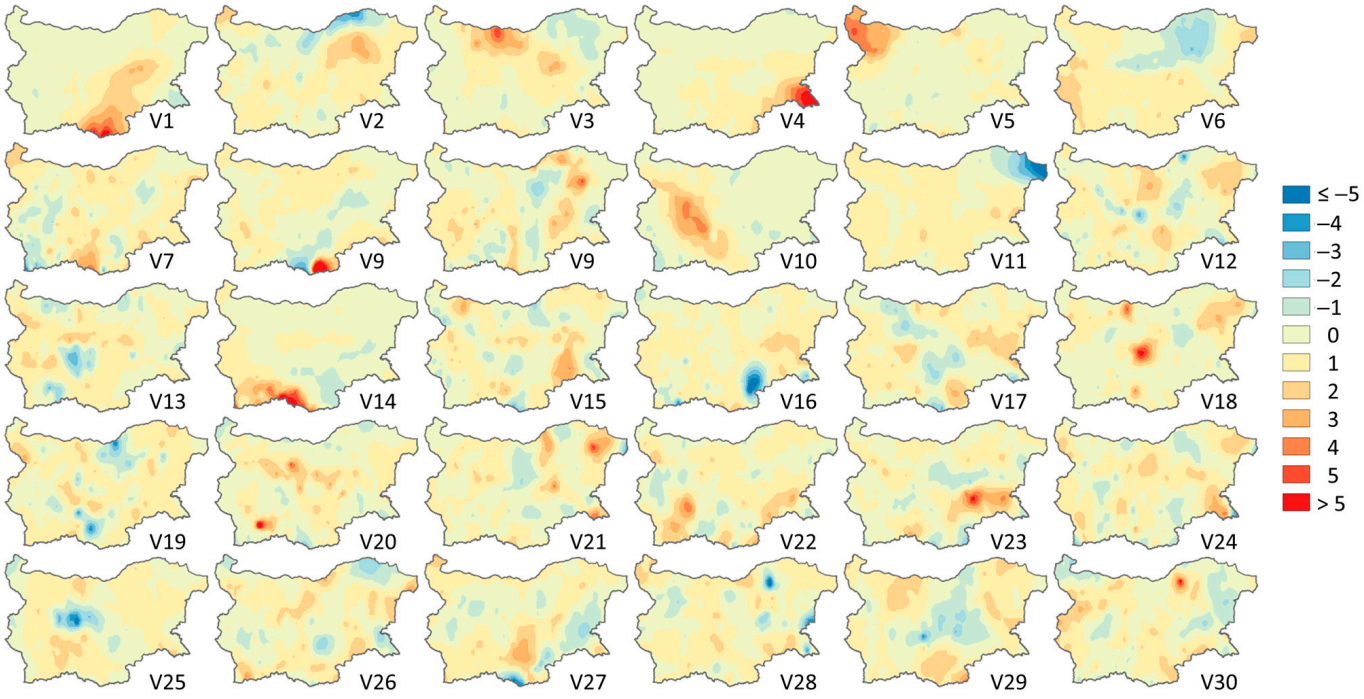


Figure A4. Spatial patterns of rotated PC scores; principal components are denoted V1 to V30; for spatial interpolation, the ordinary kriging method is used (R package "automap").

References

1. Masson-Delmotte, V.; Zhai, P.; Pirani, A.; Connors, S.; Péan, C.; Berger, S.; Caud, N.; Chen, Y.; Goldfarb, L.; Gomis, M.; et al. Climate Change 2021: The Physical Science Basis. In *Contribution of Working Group I to the Sixth Assessment Report of the Intergovernmental Panel on Climate Change*; Technical Report; IPCC: Geneva, Switzerland, 2021.
2. Myhre, G.; Alterskjær, K.; Stjern, C.W.; Hodnebrog, Ø.; Marelle, L.; Samset, B.H.; Sillmann, J.; Schaller, N.; Fischer, E.; Schulz, M.; et al. Frequency of extreme precipitation increases extensively with event rareness under global warming. *Sci. Rep.* **2019**, *9*, 16063. [CrossRef] [PubMed]
3. Zittis, G.; Almazroui, M.; Alpert, P.; Ciais, P.; Cramer, W.; Dahdal, Y.; Fnais, M.; Francis, D.; Hadjinicolaou, P.; Howari, F.; et al. Climate change and weather extremes in the Eastern Mediterranean and Middle East. *Rev. Geophys.* **2022**, *60*, e2021RG000762. [CrossRef]
4. Coopersmith, E.J.; Minsker, B.S.; Sivapalan, M. Patterns of regional hydroclimatic shifts: An analysis of changing hydrologic regimes. *Water Resour. Res.* **2014**, *50*, 1960–1983. [CrossRef]
5. Thackeray, C.W.; Hall, A.; Norris, J.; Chen, D. Constraining the increased frequency of global precipitation extremes under warming. *Nat. Clim. Chang.* **2022**, *12*, 441–448. [CrossRef]
6. Haslinger, K.; Breinl, K.; Pavlin, L.; Pistotnik, G.; Bertola, M.; Olefs, M.; Greilinger, M.; Schöner, W.; Blöschl, G. Increasing hourly heavy rainfall in Austria reflected in flood changes. *Nature* **2025**, *639*, 667–672. [CrossRef] [PubMed]
7. Kotz, M.; Levermann, A.; Wenz, L. The effect of rainfall changes on economic production. *Nature* **2022**, *601*, 223–227. [CrossRef]

8. Ionita, M.; Nagavciuc, V. Extreme Floods in the Eastern Part of Europe: Large-Scale Drivers and Associated Impacts. *Water* **2021**, *13*, 1122. [CrossRef]
9. Tichavský, R.; Ballesteros-Cánovas, J.A.; Šilhán, K.; Tolasz, R.; Stoffel, M. Dry Spells and Extreme Precipitation are The Main Trigger of Landslides in Central Europe. *Sci. Rep.* **2019**, *9*, 14560. [CrossRef]
10. Contractor, S.; Donat, M.G.; Alexander, L.V. Changes in Observed Daily Precipitation over Global Land Areas since 1950. *J. Clim.* **2021**, *34*, 3–19. [CrossRef]
11. Mascaro, G.; Farris, S.; Deidda, R. Evidence of emerging increasing trends in observed subdaily heavy precipitation frequency in the United States. *Geophys. Res. Lett.* **2025**, *52*, e2024GL114292. [CrossRef]
12. André, J.; D'Andrea, F.; Drobinski, P.; Muller, C. Regimes of precipitation change over Europe and the Mediterranean. *J. Geophys. Res. Atmos.* **2024**, *129*, e2023JD040413. [CrossRef]
13. Luppichini, M.; Bini, M.; Giannecchini, R.; Zanchetta, G. High-resolution spatial analysis of temperature influence on the rainfall regime and extreme precipitation events in north-central Italy. *Sci. Total Environ.* **2023**, *880*, 163368. [CrossRef]
14. Robinson, A.; Lehmann, J.; Barriopedro, D.; Rahmstorf, S.; Coumou, D. Increasing heat and rainfall extremes now far outside the historical climate. *npj Clim. Atmos. Sci.* **2021**, *4*, 45. [CrossRef]
15. Chen, Y.; Zhang, S.; Wang, H.; Chen, D.; Liu, J. Human-induced climate change intensifies extreme precipitation events in central China's urban areas. *Geophys. Res. Lett.* **2025**, *52*, e2024GL111818. [CrossRef]
16. Hiraga, Y.; Watanabe, S.; Yamashita, T.; Takizawa, H. Climate Change Effects on Probable Maximum Precipitation (PMP) of Mesoscale Convective Systems: Model-based Estimation and Large Ensemble-based Frequency Analysis. *J. Hydrol.* **2025**, *661*, 133724. [CrossRef]
17. Vicente-Serrano, S.M.; Tramblay, Y.; Reig, F.; González-Hidalgo, J.C.; Beguería, S.; Brunetti, M.; Kalin, K.C.; Patalen, L.; Kržič, A.; Lionello, P.; et al. High temporal variability not trend dominates Mediterranean precipitation. *Nature* **2025**, *639*, 658–666. [CrossRef]
18. Dyrrdal, A.V.; Olsson, J.; Médus, E.; Arnbjerg-Nielsen, K.; Post, P.; Aņiskeviča, S.; Thorndahl, S.; Førland, E.; Wern, L.; Mačiulytė, V.; et al. Observed changes in heavy daily precipitation over the Nordic-Baltic region. *J. Hydrol. Reg. Stud.* **2021**, *38*, 100965. [CrossRef]
19. Drobinski, P.; Silva, N.D.; Panthou, G.; Bastin, S.; Muller, C.; Ahrens, B.; Borga, M.; Conte, D.; Fosser, G.; Giorgi, F.; et al. Scaling precipitation extremes with temperature in the Mediterranean: Past climate assessment and projection in anthropogenic scenarios. *Clim. Dyn.* **2018**, *51*, 1237–1257. [CrossRef]
20. Hochman, A.; Marra, F.; Messori, G.; Pinto, J.G.; Raveh-Rubin, S.; Yosef, Y.; Zittis, G. Extreme weather and societal impacts in the eastern Mediterranean. *Earth Syst. Dynam.* **2022**, *13*, 749–777. [CrossRef]
21. Mastrantonas, N.; Herrera-Lormendez, P.; Magnusson, L.; Pappenberger, F.; Matschullat, J. Extreme precipitation events in the Mediterranean: Spatiotemporal characteristics and connection to large-scale atmospheric flow patterns. *Int. J. Climatol.* **2021**, *41*, 2710–2728. [CrossRef]
22. Silvestri, L.; Saraceni, M.; Bongioannini Cerlini, P. Links between precipitation, circulation weather types and orography in central Italy. *Int. J. Climatol.* **2022**, *42*, 5807–5825. [CrossRef]
23. Zittis, G.; Bruggeman, A.; Lelieveld, J. Revisiting future extreme precipitation trends in the Mediterranean. *Weather Clim. Extrem.* **2021**, *34*, 100380. [CrossRef]
24. Tolika, K.; Traboulsi, M.; Anagnostopoulou, C.; Zaharia, L.; Tegoulias, I.; Constantin, D.M.; Maheras, P. On the Examination of the Relationship between Mean and Extreme Precipitation and Circulation Types over Southern Romania. *Atmosphere* **2023**, *14*, 1345. [CrossRef]
25. Neykov, N.; Neytchev, P.; Zucchini, W.; Hristov, H. Linking atmospheric circulation to daily precipitation patterns over the territory of Bulgaria. *Environ. Ecol. Stat.* **2012**, *19*, 249–267. [CrossRef]
26. Lolis, C.J. High-resolution precipitation over the southern Balkans. *Clim. Res.* **2012**, *55*, 167–179. [CrossRef]
27. Houssos, E.E.; Lolis, C.J.; Bartzokas, A. Atmospheric circulation patterns associated with extreme precipitation amounts in Greece. *Adv. Geosci.* **2008**, *17*, 5–11. [CrossRef]
28. Tsonevsky, I.; Campins, J.; Genovés, A.; Jansà, A. Atmospheric patterns for heavy precipitation in Bulgaria. *Rom. J. Meteorol.* **2010**, *10*, 1–12. Available online: http://rjm.inmh.ro/2010.html (accessed on 27 January 2026).
29. Philipp, A.; Beck, C.; Huth, R.; Jacobeit, J. Development and comparison of circulation type classifications using the COST 733 dataset and software. *Int. J. Climatol.* **2016**, *36*, 2673–2691. [CrossRef]
30. Huth, R.; Beck, C.; Kučerová, M. Synoptic-climatological evaluation of the classifications of atmospheric circulation patterns over Europe. *Int. J. Climatol.* **2016**, *36*, 2710–2726. [CrossRef]
31. Ramos, A.M.; Barriopedro, D.; Dutra, E. Circulation weather types as a tool in atmospheric, climate, and environmental research. *Front. Environ. Sci.* **2015**, *3*, 151148. [CrossRef]
32. Vicente-Serrano, S.M.; López-Moreno, J.I. The influence of atmospheric circulation at different spatial scales on winter drought variability through a semi-arid climatic gradient in Northeast Spain. *Int. J. Climatol.* **2006**, *26*, 1427–1453. [CrossRef]

33. Jones, P.D.; Hulme, M.; Briffa, K.R. A comparison of Lamb circulation types with an objective classification scheme. *Int. J. Climatol.* **1993**, *13*, 655–663. [CrossRef]
34. Otero, N.; Sillmann, J.; Butler, T. Assessment of an extended version of the Jenkinson–Collison classification on CMIP5 models over Europe. *Clim. Dyn.* **2018**, *50*, 1559–1579. [CrossRef]
35. Trigo, R.M.; DaCamara, C.C. Circulation weather types and their influence on the precipitation regime in Portugal. *Int. J. Climatol.* **2000**, *20*, 1559–1581. [CrossRef]
36. Fernández-Granja, J.A.; Brands, S.; Bedia, J.; Casanueva, A.; Fernández, J. Exploring the limits of the Jenkinson–Collison weather types classification scheme: A global assessment based on various reanalyses. *Clim. Dyn.* **2023**, *61*, 1829–1845. [CrossRef]
37. Fernández-Granja, J.A.; Casanueva, A.; Bedia, J.; Fernández, J. Improved atmospheric circulation over Europe by the new generation of CMIP6 earth system models. *Clim. Dyn.* **2021**, *56*, 3527–3540. [CrossRef]
38. Cortesi, N.; Trigo, R.M.; Gonzalez-Hidalgo, J.C.; Ramos, A.M. Modelling monthly precipitation with circulation weather types for a dense network of stations over Iberia. *Hydrol. Earth Syst. Sci.* **2013**, *17*, 665–678. [CrossRef]
39. Putniković, S.; Tošić, I. Relationship between atmospheric circulation weather types and seasonal precipitation in Serbia. *Meteorol. Atmos. Phys.* **2018**, *130*, 393–403. [CrossRef]
40. Baltaci, H.; Kindap, T.; Ünal, A.; Karaca, M. The influence of atmospheric circulation types on regional patterns of precipitation in Marmara (NW Turkey). *Theor. Appl. Climatol.* **2017**, *127*, 563–572. [CrossRef]
41. Akkoyunlu, B.O.; Baltaci, H.; Tayanc, M. Atmospheric conditions of extreme precipitation events in western Turkey for the period 2006–2015. *Nat. Hazards Earth Syst. Sci.* **2019**, *19*, 107–119. [CrossRef]
42. Stoev, K.; Stoycheva, A.; Guerova, G. Foehn Climatology and Index for Sofia 1993–2014. *C. R. Acad. Bulg. Sci.* **2025**, *78*, 92–100. [CrossRef]
43. Stoev, K.; Post, P.; Guerova, G. Synoptic circulation patterns associated with foehn days in Sofia: 1979–2014. *Idojaras* **2022**, *126*, 545–560. [CrossRef]
44. Penov, N.; Stoycheva, A.; Guerova, G. Fog at Sofia 2010–2019: Objective circulation classification and fog indices. *Atmosphere* **2023**, *14*, 773. [CrossRef]
45. Ilieva, R.; Stoev, K.; Guerova, G. Climatology and circulation classification of Saharan dust over Bulgaria. *J. Atmos. Terr. Phys.* **2025**, *267*, 106403. [CrossRef]
46. Tsalova, S.; Stoycheva, A.; Stoev, K.; Guerova, G. Severe Weather Warnings for Sofia, Bulgaria: May–September 2010–2019. *C. R. Acad. Bulg. Sci.* **2024**, *77*, 1013–1021. [CrossRef]
47. Bocheva, L.; Pophristov, V. Seasonal analysis of large-scale heavy precipitation events in Bulgaria. *AIP Conf. Proc.* **2019**, *2075*, 200017. [CrossRef]
48. Bocheva, L.; Nikolova, T.; Gospodinov, I.; Simeonov, P. Large-Scale Severe Storms in Bulgaria: Seasonal Distribution and Severity. In Proceedings of the 15th International Multidisciplinary Scientific GeoConference SGEM 2015, Albena, Bulgaria, 16–25 June 2015; pp. 827–834.
49. Kalnay, E.M.; Kanamitsu, R.; Kistler, W.; Collins, D.; Deaven, L.; Gandin, M.; Iredell, S.; Saha, G.; White, J.; Woollen, Y.; et al. The NCEP/NCAR 40—Year Reanalysis Project. *Bull. Amer. Meteor. Soc.* **1996**, *77*, 437–471. Available online: https://www.eorc.jaxa.jp/ALOS/en/dataset/aw3d30/aw3d30_e.htm (accessed on 2 April 2025). [CrossRef]
50. R Core Team. *A Language and Environment for Statistical Computing*; Technical Report; R Foundation for Statistical Computing: Vienna, Austria, 2024. Available online: https://www.R-project.org/ (accessed on 2 April 2025).
51. RStudio Team. *RStudio: Integrated Development for R*; Technical Report; RStudio, Inc.: Boston, MA, USA, 2024. Available online: http://www.rstudio.com/ (accessed on 2 April 2025).
52. QGIS Development Team. *QGIS Geographic Information System*; Technical Report; Open Source Geospatial Foundation Project: Beaverton, OR, USA, 2023. Available online: http://www.qgis.org/ (accessed on 2 April 2025).
53. JAXA EORC. *ALOS Global Digital Surface Model: "ALOS World 3D-30m (AW3D30)"*; Japan Aerospace Exploration Agency Earth Observation Research Center: Tokyo, Japan, 2021. Available online: https://www.eorc.jaxa.jp/ALOS/en/dataset/aw3d30/aw3d30_e.htm (accessed on 2 April 2025).
54. Hiemstra, P.; Pebesma, E.; Twenhofel, C.; Heuvelink, G. Real-time automatic interpolation of ambient gamma dose rates from the Dutch Radioactivity Monitoring Network. *Comput. Geosci.* **2009**, *35*, 1711–1721. [CrossRef]
55. Hijmans, R.J. Terra: Spatial Data Analysis; R Package Version 1.8-29. 2020. Available online: https://cran.r-project.org/web/packages/terra (accessed on 2 April 2025).
56. Geiger, R. Klassifikation der Klimate nach W. Köppen. In *Landolt-Börnstein–Zahlenwerte und Funktionen aus Physik, Chemie, Astronomie, Geophysik und Technik*; Schäfer, K., Ed.; Springer: Berlin, Germany, 1954; Volume 3, pp. 603–607.
57. Malcheva, K.; Bocheva, L. Assessment of Contemporary Climate Change in Bulgaria Using the Köppen-Geiger Climate Classification. In *Environmental Protection and Disaster Risks*; EnviroRISKs 2022; Dobrinkova, N., Nikolov, O., Eds.; Springer: Cham, Switzerland, 2023; Lecture Notes in Networks and Systems; Volume 638, pp. 137–148. [CrossRef]

58. Cramer, W.; Guiot, J.; Marini, K. *Climate and Environmental Change in the Mediterranean Basin—Current Situation and Risks for the Future; MedECC: First Mediterranean Assessment Report*; Technical Report; UNEP/MAP: Marseille, France, 2020.
59. Twardosz, R.; Walanus, A.; Guzik, I. Warming in Europe: Recent Trends in Annual and Seasonal temperatures. *Pure Appl. Geophys.* **2021**, *178*, 4021–4032. [CrossRef]
60. Malcheva, K.; Chervenkov, H.; Bocheva, L. The importance of seasonal climate assessments in the analysis of the contemporary climate of Bulgaria. *Bulg. J. Meteorol. Hydrol.* **2023**, *27*, 1–53. (In Bulgarian)
61. Bocheva, L.; Malcheva, K. Climatological assessment of extreme 24-hour precipitation in Bulgaria during the period 1931–2019. In Proceedings of the 20th International Multidisciplinary Scientific GeoConference SGEM, Albena Resort, Bulgaria, 18–24 August 2020; Volume 20, pp. 357–364. [CrossRef]
62. Stanev, S.; Kyuchukova, M.; Lingova, S. *The Climate in Bulgaria*, 1st ed.; Publishing House of the Bulgarian Academy of Sciences: Sofia, Bulgaria, 1991. (In Bulgarian)
63. NIMH. *Monthly Hydrometeorological Bulletin (1992–2025)*; National Institute of Meteorology and Hydrology: Sofia, Bulgaria, 2025. Available online: https://bulletins.cfd.meteo.bg/ (accessed on 2 April 2025). (In Bulgarian)
64. WMO. *Guidelines on Climate Metadata and Homogenization*; WMO-TD No. 1186; World Meteorological Organization: Geneva, Switzerland, 2017.
65. WMO. *Guidelines on the Calculation of Climate Normals*; WMO-No. 1203; World Meteorological Organization: Geneva, Switzerland, 2017.
66. Stoycheva, A.; Popova, M.; Kirilova, A.; Stoev, K.; Etropolska, I.; Georgiev, C. Severe weather forecast at NIMH. In Proceedings of the Second National Congress of Physical Sciences, Sofia, Bulgaria, 25–29 September 2013. (In Bulgarian)
67. EUMETNET–MeteoAlarm. Available online: http://www.meteoalarm.org (accessed on 2 April 2025).
68. NCEP-NCAR Reanalysis 1. *Data*; NOAA PSL: Boulder, CO, USA, 2025. Available online: https://psl.noaa.gov (accessed on 2 April 2025).
69. Otero, N. Jcext: Extended Classification of Weather Types; R Package Version 0.1.1. 2022. Available online: https://CRAN.R-project.org/package=jcext (accessed on 2 April 2025).
70. White, D.; Richman, M.; Yarnal, B. Climate regionalization and rotation of principal components. *Int. J. Climatol.* **1991**, *11*, 1–25. [CrossRef]
71. Esteban, P.; Martin-Vide, J.; Mases, M. Daily atmospheric circulation catalogue for western Europe using multivariate techniques. *Int. J. Climatol.* **2006**, *26*, 1501–1515. [CrossRef]
72. Jolliffe, I.T.; Cadima, J. Principal component analysis: A review and recent developments. *Phil. Trans. R. Soc. A* **2016**, *374*, 20150202. [CrossRef]
73. Gong, X.; Richman, M.B. On the Application of Cluster Analysis to Growing Season Precipitation Data in North America East of the Rockies. *J. Clim.* **1995**, *8*, 897–931. [CrossRef]
74. Hartigan, J.A.; Wong, M.A. A K-Means Clustering Algorithm. *J. R. Stat. Soc. C Appl. Stat.* **1979**, *28*, 100–108. [CrossRef]
75. Charrad, M.; Ghazzali, N.; Boiteau, V.; Niknafs, A. NbClust: An R Package for Determining the Relevant Number of Clusters in a Data Set. *J. Stat. Softw.* **2014**, *61*, 1–36. [CrossRef]
76. Hunter, J.D. Matplotlib: A 2D Graphics Environment. *Comput. Sci. Eng.* **2007**, *9*, 90–95. [CrossRef]
77. Mills, G.F. Principal Component Analysis of precipitation and rainfall regionalization in Spain. *Theor. Appl. Climatol.* **1995**, *50*, 169–183. [CrossRef]
78. Nita, I.A.; Liviu, A.; Patriche, C.L.; Sfîcă, L.; Bojariu, R.; Birsan, M.V. Frequency of atmospheric circulation types over Romania according to Jenkinson-Collison method based on two long-term reanalysis datasets. *Rom. J. Phys.* **2022**, *67*, 812.
79. Peneva, E.; Matov, M.; Tsekov, M. Mediterranean Influence on the Climatic Regime over the Balkan Peninsula from 1901–2021. *Climate* **2023**, *11*, 68. [CrossRef]
80. Stathis, D.; Ivanova, D.; Balafoutis, C.; Makrogiannis, T. Orographic effect on heavy rainfall in Chalkidiki peninsula (Greece) induced by a Mediterranean cold front: A case study on 7 to 8 October 2000. *Croat. Meteorol. J.* **2005**, *40*, 490–493.
81. Lionello, P.; Trigo, I.F.; Gil, V.; Liberato, M.L.R.; Nissen, K.M.; Pinto, J.G.; Raible, C.C.; Reale, M.; Tanzarella, A.; Trigo, R.M.; et al. Objective climatology of cyclones in the Mediterranean region: A consensus view among methods with different system identification and tracking criteria. *Tellus A Dyn. Meteorol. Oceanogr.* **2016**, *68*, 29391. [CrossRef]
82. Caian, M.; Georgescu, F.; Pietrisi, M.; Catrina, O. Recent Changes in Storm Track over the Southeast Europe: A Mechanism for Changes in Extreme Cyclone Variability. *Atmosphere* **2021**, *12*, 1362. [CrossRef]
83. Barthlott, C.; Corsmeier, U.; Meißner, C.; Braun, F.; Kottmeier, C. The influence of mesoscale circulation systems on triggering convective cells over complex terrain. *Atmos. Res.* **2006**, *81*, 150–175. [CrossRef]
84. Insua-Costa, D.; Lemus-Cánovas, M.; Miguez-Macho, G.; Llasat, M.C. Climatology and ranking of hazardous precipitation events in the western Mediterranean area. *Atmos. Res.* **2021**, *255*, 105521. [CrossRef]

85. Olmo, M.E.; Cos, P.; Campos, D.; Muñoz, Á.G.; Altava-Ortiz, V.; Barrera-Escoda, A.; Jury, M.; Loosveldt-Tomas, S.; Bretonniere, P.; Doblas-Reyes, F.; et al. Filtering CMIP6 models in the Euro-Mediterranean based on a circulation patterns approach. *Weather Clim. Extrem.* **2025**, *48*, 100765. [CrossRef]
86. Satyanarayana, P.; Srinivas, V.V. Regional frequency analysis of precipitation using large-scale atmospheric variables. *J. Geophys. Res. Atmos.* **2008**, *113*, D24110. [CrossRef]
87. Oyler, J.W.; Nicholas, R.E. Time of observation adjustments to daily station precipitation may introduce undesired statistical issues. *Int. J. Climatol.* **2018**, *38*, e364–e377. [CrossRef]
88. Becherini, F.; Stefanini, C.; della Valle, A.; Rech, F.; Zecchini, F.; Camuffo, D. Adjustment Methods Applied to Precipitation Series with Different Starting Times of the Observation Day. *Atmosphere* **2024**, *15*, 412. [CrossRef]
89. Cureton, E.E.; D'Agostino, R.B. *Factor Analysis: An Applied Approach*, 1st ed.; L. Erlbaum Associates: Hillsdale, NJ, USA, 1983.
90. Kaiser, H.F. The varimax criterion for analytic rotation in factor analysis. *Psychometrika* **1958**, *23*, 187–200. [CrossRef]
91. Richman, M.B. Rotation of principal components. *J. Climatol.* **1986**, *6*, 293–335. [CrossRef]

Disclaimer/Publisher's Note: The statements, opinions and data contained in all publications are solely those of the individual author(s) and contributor(s) and not of MDPI and/or the editor(s). MDPI and/or the editor(s) disclaim responsibility for any injury to people or property resulting from any ideas, methods, instructions or products referred to in the content.